Univerzita Karlova v Praze
Matematicko-fyzikální fakulta

DIPLOMOVÁ PRÁCE

Kryštof Touška

Matematické modelování viskoplastických materiálů

Matematický ústav UK

Vedoucí diplomové práce:	RNDr. Ing. Jaroslav Hron Ph.D.
Studijní program:	Fyzika
Studijní obor:	Matematické a počítačové modelování ve fyzice a technice

Praha 2012

Charles University in Prague
Faculty of Mathematics and Physics

MASTER THESIS

Kryštof Touška

Mathematical modeling of visco-plastic materials

Mathematical Institute of Charles University

Supervisor of the master thesis:	RNDr. Ing. Jaroslav Hron Ph.D.
Study programme:	Physics
Specialization:	Mathematical and Computer Modelling in Physics and Engineering

Prague 2012

I would like to express my deepest thanks to my supervisor RNDr. Ing. Jaroslav Hron, Ph.D for his guidance, provided software, articles and his will to help. I offer my sincerest gratitude to prof. RNDr. Josef Málek, CSc., DSc., who has inspired me and also provided me several books, articles and ideas.

Of course I can't even tell how grateful I am to Jana and my family for their patience and support in the time of my studies.

I declare that I carried out this master thesis independently, and only with the cited sources, literature and other professional sources.

I understand that my work relates to the rights and obligations under the Act No. 121/2000 Coll., the Copyright Act, as amended, in particular the fact that the Charles University in Prague has the right to conclude a license agreement on the use of this work as a school work pursuant to Section 60 paragraph 1 of the Copyright Act.

In Prague on August 3, 2012

Název práce: Matematické modelování viskoplastických materiálů

Autor: Kryštof Touška

Katedra: Matematický ústav UK

Vedoucí diplomové práce: RNDr. Ing. Jaroslav Hron Ph.D., Matematický ústav UK

Abstrakt: Práce obsahuje v první části úvod do viskoplasticity a přehled řešených problémů. Ve druhé kapitole je odvozen konstitutivní vztah pro Binghamovu tekutinu a předveden postup důkazu existence a jednoznačnosti klasickou variační metodou. Tento postup je porovnán s postupem skrze moderní implicitní teorii. V závěrečné části je nejprve proveden přehled užitých formulací a použitý software. Následuje hlavní část s výsledky numerických simulací, jak za účelem srovnání jednotlivých přístupů, tak pro ověření zvoleného přístupu ve složitějších simulacích. Předpokládá se možná aplikace testovaných přístupů na jiné typy materiálů.

Klíčová slova: viskoplasticita, Binghamova tekutina, MKP, proudění

Title: Mathematical modeling of visco-plastic materials

Author: Kryštof Touška

Department: Mathematical Institute of Charles University

Supervisor: RNDr. Ing. Jaroslav Hron Ph.D., Mathematical Institute of Charles University

Abstract: In the first chapter of the thesis we present an introduction to the visco-plasticity and overview of the presented problems. The constitutive relation for Bingham fluid is derived and the second chapter. Further there is demonstrated a procedure of proving existence and uniqueness with classical variational method. This method is compared with the same process using modern implicit theory. The last chapter starts with summary of used problem formulations and used software. It is then followed by the main part with results of numerical simulations, both for the purpose of used formulations comparison and then verification of the preferred one in more complicated simulations. We expect a possible application of tested approaches on different materials.

Keywords: visco-plasticity, Bingham fluid, FEM, flow

Contents

Introduction

The plastic materials exhibits almost no deformation until a certain level of stress is reached - so called *yield stress*. Materials start to flow above this level. A suspensions of concentrated solid particles in Newtonian liquids exhibits a yield stress followed by almost Newtonian behaviour. These compounds are often called Bingham fluid or Bingham plastic after E. C. Bingham who studied plastic materials early in the 20th century [9]. He observed paints and described such behaviour in 1919. But not only paints, also pastes, food substances like ketchup or mayonnaise [35], petroleum [15], ice slurries [27] and industry materials as ceramics obey these laws.

It is mentioned in [28] that existence of the yield stress was a subject of many discussions in scientific community. Former investigations showed that alumina slurries exhibited only highly increased viscosity at low shear rates. Reliable data are usually available at higher shear rates and yield stress values are determined by extrapolations. Such behavior is similar to the techniques we use, however our effort is to get as close as possible to the ideal model.

Our main focus lies in the numerical implementation of several different approaches. We would like to start with standard finite elements implementation and make all the alterations on the level of problem formulation. Such process should make itself easily reproducible and also possibly usable for wider spectrum of materials. An article with the similar targets has been published in 2011 [3].

The first chapter shows why there is a need for visco-plasticity and the considered problems. In the second chapter we make a short step aside and present related existing results in the field of analysis, both classical and modern. The last chapter demonstrates numerical results. We start with a testing problem, two benchmark two real-world problems follow. At the end we devote a short section to the Herschel-Bulkley model, which might be considered as a generalization of Bingham model.

Chapter 1

Considered problems

In this chapter we would like to introduce considered problems and their role. As we want for this work to be related to real-world problems as much as possible, we present five different problems.

First three of them act as so called toy-problems and we use them mainly for testing our approach. These three problems are well suited, because of available analytical solution (Poiseuille flow) or previously published results of numerical simulations (lid-driven cavity and flow around cylinder).

Last two problems are examples of common industry situations. Also for those there were some published results that we can compare with.

But before we do that, let us say, what visco-plastic means and, in the spirit of this chapter, present some real-world examples of both materials and their application.

1.1 Elastic, plastic and visco-plastic laws

Consider a cylindrical specimen, a bar of length l_0 and cross-section S. We perform *loading experiment*, i.e. we subject the cylinder to the force $P(t)$ at both ends. The quantity σ is defined as

$$\sigma(t) = \frac{P(t)}{S} \, , \tag{1.1}$$

where σ can be interpreted as the stress. We also define the relative extension ε by the equality

$$\varepsilon(t) = \frac{l(t) - l_0}{l_0} \, . \tag{1.2}$$

If we measure both these quantities during loading experiment, we obtain *stress-strain* diagram as in Fig. 1.1.

The part between points O and A is a linear one as the relation between stress and strain really is. The *proportionality limit* denoted as σ_A can be established experimentally. Following part AB is curved, hence the stress-strain relation is no longer linear.

If we stopped increasing the force P and on the contrary we decrease it to zero, we would perform *unloading experiment*. Should this test take part for stresses low enough, the stress-strain relation is retraced along the same curve back to

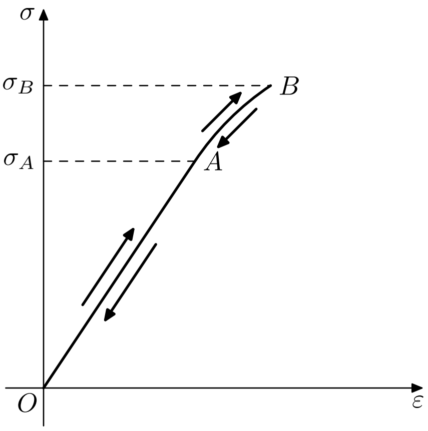

Figure 1.1: Stress-strain diagram, [25]

the point O. The linear relation is studied in the *theory of elasticity* and is called Hooke's law

$$\sigma = E\varepsilon \tag{1.3}$$

Non-linear relation can be described in the general form

$$\sigma = f(\varepsilon)\ . \tag{1.4}$$

Three dimensional equivalent of Hooke's law is

$$\sigma = \mathcal{A}\varepsilon\ , \tag{1.5}$$

where $\mathcal{A}$ is a fourth-order tensor and (1.4) takes the form

$$\sigma = F(\varepsilon)\ , \tag{1.6}$$

where F is a tensorial function.

Furthermore we extend previous loading experiment as shown in Fig. 1.2, which corresponds to steel.

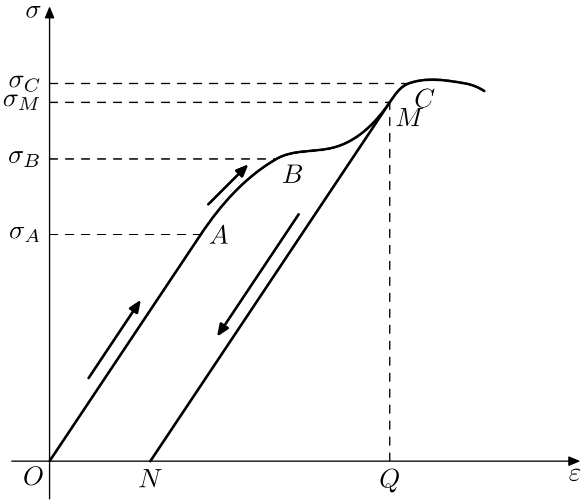

Figure 1.2: Stress-strain diagram for steel, [25]

At point B the strain increases with only a small or no change in the stress. The stress σ_B is called the *yield limit.* Following the curve up to the point C, we would reach the *strength* limit. Further stretching would break the specimen.

Regarding the unloading experiment, let us follow the loading as far as point M, where the stress σ_M exceeds yield limit σ_B. For the majority of metals the unloading would follow the MN line, which is roughly parallel to the line OA. After the experiment a part of the strain NQ vanishes and the other part ON remains permanently. The vanishing portion is called the *elastic strain* and the remaining portion is called the *plastic strain.*

Such behavior cannot be described by previous elastic laws, hence plastic constitutive laws must be derived.

The classical theory of plasticity works with stress rate and strain rate having them proportional, while the coefficient is usually a function of the stress, the strain and the strain rate.

$$\dot{\sigma} = \mathcal{E}(\sigma, \varepsilon, \dot{\varepsilon})\dot{\varepsilon} \ . \tag{1.7}$$

Classical plasticity theory presumes that the coefficient $\mathcal{E}$ is a positively homogeneous function in its last argument, hence a theory based on a (1.7) is a time-independent theory. Constitutive law retains its form after a change in the time variable $\tau = h(t)$.

An example of plastic constitutive law with a domain of elastic behaviour can be

$$\mathcal{E}(\sigma, \varepsilon, \dot{\varepsilon}) = \begin{cases} E & \text{if } |\sigma| < \sigma_Y \text{ or } (|\sigma| = \sigma_Y \text{ and } \sigma \cdot \dot{\varepsilon} < 0) \\ 0 & \text{if } |\sigma| = \sigma_Y \text{ and } \sigma \cdot \dot{\varepsilon} \geq 0 \ , \end{cases} \tag{1.8}$$

where σ_Y is the yield limit. This model is called a *perfectly plastic model.*

Now let us stop loading experiment at the point P in Fig. 1.3. The stress is to be held on a constant level, a soft testing machine would allow us to do so. In a long time interval a slow increase of strain can be observed. Direction PQ in Fig. 1.3 represents such phenomenon called the *creep.*

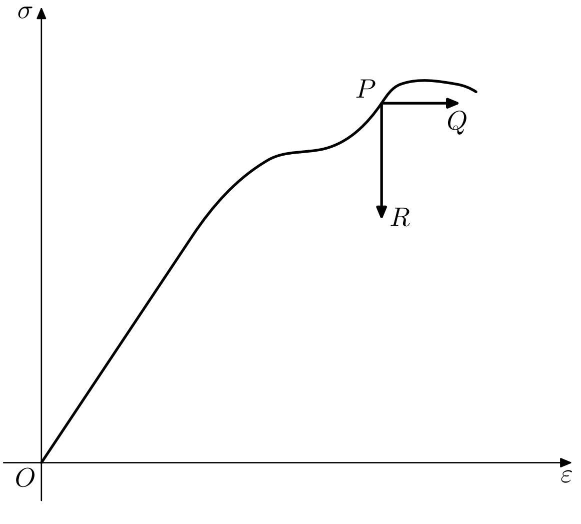

Figure 1.3: Long-range test (creep and relaxation), [25]

A creep strain-time diagram is presented in Fig. 1.4. For small applied stresses the strain is going to stabilize, it has a horizontal asymptote. However should the applied stress exceed a certain limit, the strain-time curve is strictly increasing and the specimen is going to break.

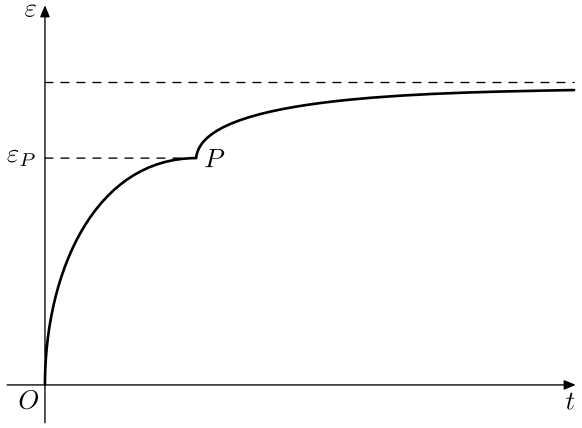

Figure 1.4: Time evolution of strain during the creep phenomenon, [25]

Instead of soft testing machine, one could use a hard testing machine for diagnostic tests. In the point P in Fig. 1.3 the strain is maintained constant, while the stress can be measured. Unlike the strain during the creep test, the stress decreases in time. The time interval of the decreasing is much longer than those in unloading experiments. This decrease is called *relaxation.* The stress would follow the direction PR in Fig. 1.3, its time dependency is shown in Fig. 1.5.

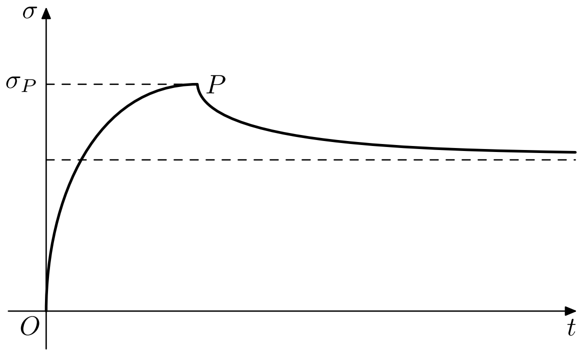

Figure 1.5: Time evolution of stress during the relaxation phenomenon, [25]

Given the relaxation phenomenon the stress can decrease almost to zero, or the curve in Fig. 1.5 may tend to a horizontal asymptote. The asymptote location depends on the initial stress-strain state.

The creep phenomenon and the relaxation phenomenon cannot be described neither by elastic constitutive laws nor by the plastic constitutive laws. To describe these phenomena, more advanced constitutive laws were developed, for example *rate-type viscoplastic laws.*

Further in the text are concerned mainly with the model of the Bingham fluid. Constitutive equations are derived in the section 2.1.1. Such fluid omits elastic behaviour and rather presents rigid-body behaviour, which changes into viscous flow after exceeding yield stress. E.C. Bingham described paint in this way in 1919 and further continued with the model in [9]. These materials were analyzed by Oldroyd [32], [33], Reiner [39] and Prager [36]. Apart from paints, [22] mentions also slurries, pastes, and food substances are examples of Bingham plastics. Another example is a toothpaste that behaves like a rigid body at rest inside the tube. While being pressed out, it flows with a certain level of viscosity and finally it retains its shape outside the tube.

Figure 1.6: Toothpaste, [46]

The material presented in this section is standard and can be found in [25], [16] and [35].

1.2 Poiseuille flow

Poiseuille flow is one of the simplest examples of Bingham fluid flows. Yet it can be very useful object of studies, mainly for two reasons. The first one is that the analytical solution is available, hence we can evaluate the achieved precision of our simulations in terms of L_2 error, but also in its main characteristics as the maximal velocity ($\|u\|_\infty$) or a width of an unyielded region. The other reason is that the Poiseuille flow of the Bingham fluid is often a part of larger problems, both in real world, such as flows in cooling systems (see [19]), and also in numerical simulations, like a pressure driven flow around cylinder in [47].

Poiseuille flow is a pressure driven flow between two parallel plates, which are stationary. A no-slip boundary condition is prescribed on the plates.

Such flow of Bingham fluid has several interesting properties. Unlike the case of the Newtonian fluid, the velocity profile isn't parabolic in the entire width of the channel, but rather exhibits a rigid body, often called a *plug*, moving with the fluid in the middle section. A simple visualisation is on the Fig. 1.7. The flow is also known to cease in a finite time after removing the acting pressure, more details of this phenomenon can be found in [14].

1.3 Lid-driven cavity

If we had to name the most common testing problem for viscoplastic flows, it would be a lid-driven cavity. A well known test has been used as a validation for

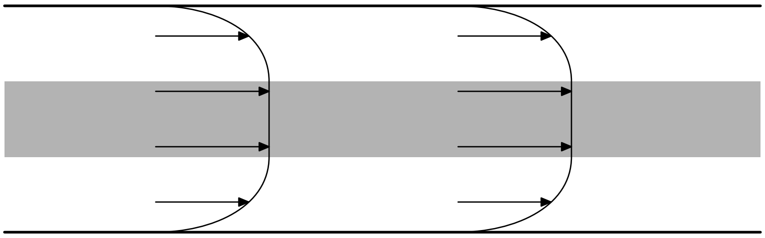

Figure 1.7: Poisseuille flow

many codes and solution methods.

Lid-driven cavity geometry is a unit square. The boundary conditions are simple enough as well, a tangential velocity is prescribed on the top boundary and the other three sides are motionless. Of course difficulties with the discontinuity of boundary conditions arise, some authors regularize the velocity on the top boundary as in [18], while the others rely on the interpolation on the element edge, see also [18] or [30].

There are many results for Bingham fluid, mostly they omit convective term and concentrate on the Stokes problem. Usually the presented results, see [45], [30], [3], [18], include the growth of the unyielded region with higher yield stress level and the vortex position and intensity.

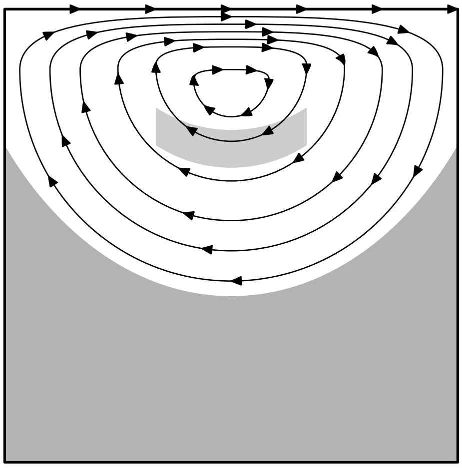

Figure 1.8: Lid-driven cavity

List of additional resources for the original problem can be found in [13].

1.4 Flow around cylinder

A flow of a fluid around cylinder has been studied already by Stokes in 1850, [42]. His article presented so called *Stokes paradox*. He concluded that with certain restrictions such flow would never be a steady state flow. Many articles has been written on the topic, one of the recent [44] states, that the setting led to an ill-posed problem, because one cannot assume to be at infinite distance from an infinite cylinder.

For the purpose of numerical simulations many different settings have been studied, for example [20] features results for Newtonian fluid including high precision values of drag and lift coefficients of forces acting on the cylinder and also a pressure difference on the cylinder.

In the case of Bingham fluid let us mention two articles by Mitsoulis [29] and Mitsoulis and Zisis [47]. Their results include large scale of yield stresses and also different geometrical settings. Besides the unyielded region, a drag coefficient progress is also calculated.

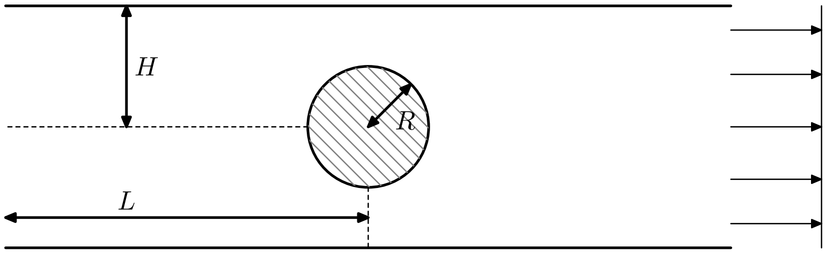

Figure 1.9: Flow around cylinder

1.5 Wire-drawing problem

Wire-drawing is a metalworking process for reducing diameter of a wire by pulling it through a die or a series of dies. According to [1], wire was originally made by cutting strips from plates and afterwards rounded by beating. Wire-drawing became known in the 14th century.

Modern wiring machines consists of many dies, area reduction is up to 30% per drawing pass. To lessen the wear on surface, the wires are lubricated with oil, soapy water or sulphates. For more details about wire-drawing, see [43].

[25] models wire going through a die as a Bingham fluid, similar setting is used for our problem, geometrical setting can be seen in Fig. 1.10.

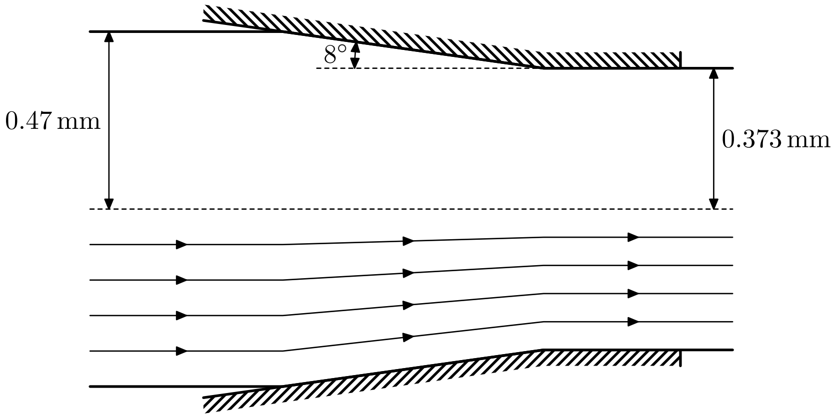

Figure 1.10: Wire-drawing

1.6 Tape-casting unit

Many ceramic products for electronics industry are made by tape-casting technology. It has been developed in the 1940s for producing miniaturized capacitors. Current products examples are microcapacitors or covers for integrated circuits. A whole chapter about tape-casting can be found in [40].

A schematic example of tape-casting machine is in Fig. 1.11. It consists of an open reservoir on the left side and the channel on the bottom. A belt with constant speed runs under the channel.

This machine has been thoroughly studied in [28]. Both experimental and computed date are presented, which make basis for our simulation results evaluation. For the process itself, the fluid is a mixture of α-Al_2O_3 powder, cellulose acetate, dibutyl phthalate, fish oil, acetone and cyclo-hexanone. We aim to reproduce the shape of the free surface as well as to find unyielded regions in the reservoir for different belt speeds.

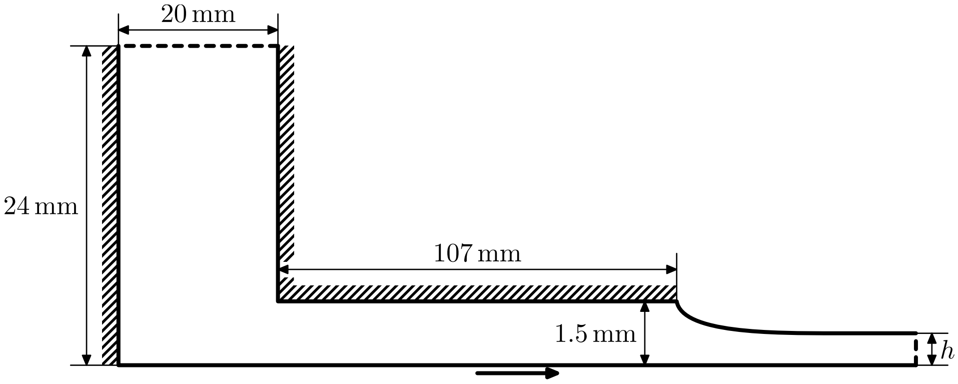

Figure 1.11: Tape-casting machine

Chapter 2

Analysis of the problems

Our main concern lies in the numerical simulations, but even though we would to include some existing results to include necessary part of mathematical modelling and also to compare two different approaches, both related to the constitutive relations we use.

2.1 Classical approach

We start with classical variational approach. Firstly we derive constitutive equation for Bingham fluid and later we show existence and uniqueness for the Stokes problem. Whole section follows first part of the fifth chapter in [25].

2.1.1 Bingham fluid

We shall start by deriving the constitutive equation of the Bingham fluid. We denote the symmetric part of velocity gradient as $\boldsymbol{D}$,

$$\boldsymbol{D} = \frac{1}{2}\left(\nabla \boldsymbol{u} + \nabla^T \boldsymbol{u}\right) \tag{2.1}$$

and its deviator with a prime,

$$\boldsymbol{D}' = \boldsymbol{D} - \frac{1}{3}\left(\operatorname{tr} \boldsymbol{D}\right) \boldsymbol{I} \ . \tag{2.2}$$

We denote Cauchy stress tensor $\boldsymbol{T}$ and analogously its deviator

$$\boldsymbol{T}' = \boldsymbol{T} + p\boldsymbol{I} \ . \tag{2.3}$$

Then the Bingham model for viscoplastic materials is based on the following equations

$$\boldsymbol{T}' = \boldsymbol{S} + 2\eta \boldsymbol{D}' \ , \tag{2.4}$$

$$f(\boldsymbol{S}) = |\boldsymbol{S}|^2 - g^2 \leq 0 \ , \tag{2.5}$$

$$\boldsymbol{D}' = 2\lambda \boldsymbol{S} \ . \tag{2.6}$$

η is a viscosity coefficient, g is the yield stress and λ satisfies

$$\begin{aligned} &\lambda(t) = 0 \qquad \text{if } f(\boldsymbol{S}) < 0 \text{ or } f(\boldsymbol{S}) = 0 \text{ and } \dot{f}(\boldsymbol{S}) < 0 \ , \\ &\lambda(t) > 0 \qquad \text{if } f(\boldsymbol{S}) = 0 \text{ and } \dot{f}(\boldsymbol{S}) = 0 \ . \end{aligned} \tag{2.7}$$

The equation (2.4) basically divides stress tensor deviator into plastic and viscous part. Second equation (2.5) is so called *Von Mises yield criterion*. Finally equations (2.6) and (2.7) states that the symmetric part of the velocity gradient can vary only if $\boldsymbol{S}$ is moving along the surface $f(\boldsymbol{S}) = 0$.

Usually also we assume the incompressibilty condition,

$$\operatorname{tr}\boldsymbol{D} = 0\ . \tag{2.8}$$

We simply start by putting (2.6) into (2.4),

$$\boldsymbol{T}' = (1 + 4\eta\lambda)\boldsymbol{S} \tag{2.9}$$

and also

$$|\boldsymbol{T}'| = (1 + 4\eta\lambda)|\boldsymbol{S}|\ . \tag{2.10}$$

If $|\boldsymbol{T}'| \leq g$, then either $|\boldsymbol{S}| = g$ and (2.10) implies that $\lambda = 0$ or $|\boldsymbol{S}| < g$ meaning that $f(\boldsymbol{S}) < 0$ and from (2.7) we also get $\lambda = 0$. In this case (2.6) and (2.8) give us $\boldsymbol{D} = 0$.

Let us consider $|\boldsymbol{T}'| > g$. (2.10) and (2.5) implies $\lambda > 0$. From (2.7) it follows that $f(\boldsymbol{S}) = 0$ and thus $|\boldsymbol{S}| = g > 0$. (2.10) is then equal to

$$\lambda = \frac{1}{4}\left(\frac{|\boldsymbol{T}'|}{g} - 1\right) \tag{2.11}$$

and hence from (2.6), (2.9) and (2.8) we derive

$$\boldsymbol{D} = \frac{1}{2\eta}\left(1 - \frac{g}{|\boldsymbol{T}'|}\right)\boldsymbol{T}'\ . \tag{2.12}$$

Altogether the constitutive equation of the Bingham fluid is

$$\boldsymbol{D} = \begin{cases} \frac{1}{2\eta}\left(1 - \frac{g}{|\boldsymbol{T}'|}\right)\boldsymbol{T}' & \text{if } |\boldsymbol{T}'| > g \\ 0 & \text{if } |\boldsymbol{T}'| \leq g\ . \end{cases} \tag{2.13}$$

Such constitutive relation can be inverted to more traditional form of $\boldsymbol{T}(\boldsymbol{D})$. Let $|\boldsymbol{D}| = 0$, it follows that $|\boldsymbol{T}'| \leq g$. Now let $|\boldsymbol{D}| \neq 0$, we get

$$|\boldsymbol{T}'| = 2\eta|\boldsymbol{D}| + g\ , \tag{2.14}$$

which together with (2.13) implies

$$\boldsymbol{T}' = 2\eta\boldsymbol{D} + g\frac{\boldsymbol{D}}{|\boldsymbol{D}|}\ . \tag{2.15}$$

Hence we can write

$$\left.\begin{array}{cc} \boldsymbol{T}' = 2\eta\boldsymbol{D} + g\frac{\boldsymbol{D}}{|\boldsymbol{D}|} & \text{if } |\boldsymbol{D}| \neq 0 \\ |\boldsymbol{T}'| \leq g & \text{if } |\boldsymbol{D}| = 0\ . \end{array}\right\} \tag{2.16}$$

Moreover one can invert also (2.16) and obtain (2.13), meaning that constitutive relations (2.13) and (2.16) are equivalent. (2.16) is a common form of constitutive equation of the Bingham fluid.

2.1.2 Solution existence and uniqueness

Consider the following problem in bounded domain $\Omega \subset \mathbb{R}^3$ with a smooth boundary Γ.

$$\operatorname{div} \boldsymbol{T} + \boldsymbol{b} = 0 \ , \tag{2.17}$$

$$\operatorname{div} \boldsymbol{u} = 0 \ , \tag{2.18}$$

$$\left.\begin{array}{ll} \boldsymbol{T}' = 2\eta \boldsymbol{D} + g\frac{\boldsymbol{D}}{|\boldsymbol{D}|} & \text{if } |\boldsymbol{D}| \neq 0 \\ |\boldsymbol{T}'| \leq g & \text{if } |\boldsymbol{D}| = 0 \ . \end{array}\right\} \tag{2.19}$$

$$\boldsymbol{D} = \frac{1}{2}\left(\nabla \boldsymbol{u} + \nabla^T \boldsymbol{u}\right) \ . \tag{2.20}$$

We divide Γ into disjoint parts $\Gamma = \Gamma_1 \cup \Gamma_2 \cup \Gamma_3 \cup \Gamma_4 \cup \Gamma_5$ and prescribe boundary conditions

$$\boldsymbol{u} = \boldsymbol{U} \qquad \text{on } \Gamma_1 \ , \tag{2.21}$$

$$\boldsymbol{t} = \boldsymbol{F} \qquad \text{on } \Gamma_2 \ , \tag{2.22}$$

$$\boldsymbol{u}_\tau = 0 \ \ \boldsymbol{t} \cdot \boldsymbol{\nu} = f_v \qquad \text{on } \Gamma_3 \ , \tag{2.23}$$

$$\boldsymbol{u} \cdot \boldsymbol{\nu} = 0 \ \ \boldsymbol{t}_\tau = 0 \qquad \text{on } \Gamma_4 \ , \tag{2.24}$$

$$\left.\begin{array}{l} \qquad\qquad \boldsymbol{u} \cdot \nu = 0 \\ |\boldsymbol{t}_\tau| \leq \mu S \left\{ \begin{array}{l} \text{if } |\boldsymbol{t}_\tau| < \mu S \text{ then } \boldsymbol{u}_\tau = 0 \\ \text{if } |\boldsymbol{t}_\tau| = \mu S \text{ then there exists } \lambda \geq 0 \\ \text{such that } \boldsymbol{u}_\tau = -\lambda \boldsymbol{t}_\tau \end{array}\right. \end{array}\right\} \text{on } \Gamma_5 \ . \tag{2.25}$$

$\boldsymbol{\nu}$ is the exterior unit normal of boundary Γ, stress vector $\boldsymbol{t} = \boldsymbol{T} \cdot \ \boldsymbol{\nu}$ and $\boldsymbol{u}_\tau$ is the tangential component of $\boldsymbol{u}$. Boundary condition on Γ_5 is a friction law, μ is the friction coefficient.

Let us define

$$K = \left\{ \boldsymbol{u} \in \left[H^1(\Omega)\right]^3 \mid \operatorname{div} \boldsymbol{u} = 0 \text{ in } \Omega, \boldsymbol{u}|_{\Gamma_1} = \boldsymbol{U}, \boldsymbol{u}_\tau|_{\Gamma_3} = 0, \boldsymbol{u} \cdot \boldsymbol{\nu}|_{\Gamma_4 \cup \Gamma_5} = 0 \right\} \ , \tag{2.26}$$

which is the set of admissible fields.

In addition following must be satisfied

$$K \neq \varnothing \ , \tag{2.27}$$

$$\boldsymbol{F} \in \left[L^2(\Gamma_2)\right]^3 \ , \tag{2.28}$$

$$f_\nu \in L^2(\Gamma_3) \ , \tag{2.29}$$

$$\boldsymbol{b} \in \left[L^2(\Omega)\right]^3 \ , \tag{2.30}$$

$$\mu \in L^\infty(\Gamma_5), \quad \mu \geq 0 \text{ a.e. on } \Gamma_5 \ , \tag{2.31}$$

$$S \in L^\infty(\Gamma_5), \quad S \geq 0 \text{ a.e. on } \Gamma_5 \ . \tag{2.32}$$

Before we give the variational formulation for the problem (2.17)–(2.25), let us denote several functionals

$$a : [H^1(\Omega)]^3 \times [H^1(\Omega)]^3 \to \mathbb{R}, \quad a(\boldsymbol{u}, \boldsymbol{v}) = \eta \int_\Omega \boldsymbol{D}(\boldsymbol{u}) \cdot \boldsymbol{D}(\boldsymbol{v}) \mathrm{d}x \ , \tag{2.33}$$

$$\tilde{j} : [H^1(\Omega)]^3 \to \mathbb{R}, \qquad \tilde{j}(\boldsymbol{v}) = g \int_\Omega |\boldsymbol{D}(\boldsymbol{v})| \mathrm{d}x + \int_{\Gamma_5} \mu |S| |\boldsymbol{v}_\tau| \mathrm{d}\Gamma \ , \tag{2.34}$$

$$\tilde{f} : [H^1(\Omega)]^3 \to \mathbb{R}, \qquad \tilde{f}(\boldsymbol{v}) = \int_\Omega \boldsymbol{b} \cdot \boldsymbol{v} \mathrm{d}x + \int_{\Gamma_2} \boldsymbol{F} \cdot \boldsymbol{v} \mathrm{d}\Gamma + \int_{\Gamma_3} f_\nu \boldsymbol{v} \cdot \boldsymbol{\nu} \mathrm{d}\Gamma \ , \tag{2.35}$$

$$J : [H^1(\Omega)]^3 \to \mathbb{R}, \qquad J(\boldsymbol{v}) = \frac{1}{2} a(\boldsymbol{v}, \boldsymbol{v}) + \tilde{j}(\boldsymbol{v}) - \tilde{f}(\boldsymbol{v}) \ . \tag{2.36}$$

Considering (2.27)–(2.36), for $(\boldsymbol{u}, \boldsymbol{T})$ smooth solution of the problem (2.17)–(2.25), then following inequality holds

$$\boldsymbol{u} \in K, \quad J(\boldsymbol{u}) \le J(\boldsymbol{v}) \quad \forall \boldsymbol{v} \in K \ . \tag{2.37}$$

It can be shown that the minimum point problem (2.37) holds if and only if the following variational inequality remains valid

$$\boldsymbol{u} \in K, \quad a(\boldsymbol{u}, \boldsymbol{v} - \boldsymbol{u}) + \tilde{j}(\boldsymbol{v}) - \tilde{j}(\boldsymbol{u}) \ge \langle f, \boldsymbol{v} - \boldsymbol{u} \rangle \quad \forall \boldsymbol{v} \in K \ . \tag{2.38}$$

$\langle , \rangle$ is the duality pairing between real normed space and its dual.

Further we obtain homogeneous boundary condition. With $\boldsymbol{u}_0 \in K$ we define another admissible field

$$V = K - \boldsymbol{u}_0 = \left\{ \boldsymbol{u} \in \left[H^1(\Omega) \right]^3 | \operatorname{div} \boldsymbol{u} = 0 \text{ in } \Omega, \boldsymbol{u}|_{\Gamma_1} = 0, \boldsymbol{u}_\tau|_{\Gamma_3} = 0, \boldsymbol{u} \cdot \boldsymbol{\nu}|_{\Gamma_4 \cup \Gamma_5} = 0 \right\} \ , \tag{2.39}$$

functional and element

$$j : [H^1(\Omega)]^3 \to \mathbb{R}, \qquad j(v) = \tilde{j}(\boldsymbol{v} + \boldsymbol{u}_0) \ , \tag{2.40}$$

$$f \in V', \quad \langle f, \boldsymbol{v} \rangle = \langle \tilde{f}, \boldsymbol{v} \rangle + a(\boldsymbol{u}_0, \boldsymbol{v}) \ , \tag{2.41}$$

where V' is the dual of V.

Then $\boldsymbol{u} \in K$ is a solution for the (2.38) if and only if $\bar{\boldsymbol{u}} = \boldsymbol{u} - \boldsymbol{u}_0 \in V$ solves the following inequality

$$\bar{\boldsymbol{u}} \in V, \quad a(\bar{\boldsymbol{u}}, \boldsymbol{v} - \bar{\boldsymbol{u}}) + j(\boldsymbol{v}) - j(\bar{\boldsymbol{u}}) \ge \langle f, \boldsymbol{v} - \bar{\boldsymbol{u}} \rangle \quad \forall \boldsymbol{v} \in V \ . \tag{2.42}$$

If $(\boldsymbol{u}, \boldsymbol{T})$ is a smooth solution of the original problem (2.17)–(2.25), than $\boldsymbol{u} - \boldsymbol{u}_0$ is a solution of (2.42). Hence apart for the involved translation, every solution of (2.42) is a solution of the problem (2.17)–(2.25). Because we want to apply Korn's inequality, it is necessary to suppose that

$$\operatorname{meas} \Gamma_1 > 0 \ . \tag{2.43}$$

Then if (2.27)–(2.32) holds, there exists a unique solution $\bar{\boldsymbol{u}} = \boldsymbol{u} - \boldsymbol{u}_0$ of the variational inequality (2.42).

Proofs of all statements in this subsection can be found either in [25] or many other textbooks.

2.1.3 Regularized constitutive equation

For numerical simulations we use a smooth approximation of constitutive relation (2.16), i.e.

$$\boldsymbol{T}'_\varepsilon = 2\eta \boldsymbol{D} + g \frac{\boldsymbol{D}}{\sqrt{|\boldsymbol{D}|^2 + \varepsilon^2}} \ . \tag{2.44}$$

Then, according to [18], for solutions $\boldsymbol{u}$ and $\boldsymbol{u}_\varepsilon$ of original and regularized stationary problem, we have

$$\|\boldsymbol{u}_\varepsilon - \boldsymbol{u}\|^2_{L^2\Omega} \leq \frac{g|\Omega|}{\mu\lambda_0}\varepsilon \ , \tag{2.45}$$

where $\lambda_0 > 0$ is the smallest eigenvalue of the operator $-\nabla^2$ on Ω for the homogeneous Dirichlet boundary conditions.

We have thus

$$\lim_{\varepsilon\to 0} \boldsymbol{u}_{\boldsymbol{\varepsilon}} = \boldsymbol{u} \text{ in } L^2(\Omega) \ . \tag{2.46}$$

2.2 Implicit constitutive theory

Newtonian fluids cannot exhibit several phenomena observed on many real fluids. A simplest attempt to obtain a more general model is by setting a nonlinear relation between $\boldsymbol{T}$ and $\boldsymbol{D}$. The main idea of implicit constitutive theory is to replace an explicit functional of the symmetric part of the velocity gradient $\boldsymbol{D}$

$$\boldsymbol{T} = \boldsymbol{T}(\boldsymbol{D}) \tag{2.47}$$

by the implicit relation between $\boldsymbol{T}$ and $\boldsymbol{D}$,

$$\boldsymbol{G}(\boldsymbol{T}, \boldsymbol{D}) = 0 \ . \tag{2.48}$$

Implicit constitutive theory makes a robust framework that can easily extend models by other quantities and relations. Important part for us is that it can be used not only for describing new material models with various non-linear phenomena, but it can also easily describe well known and examined effects like in our case a yield stress.

Such description of Bingham fluid [31] is

$$2\eta\boldsymbol{D}\left(g + (|\boldsymbol{T}'| - g)^+\right) = \left(|\boldsymbol{T}' - g|\right)^+ \boldsymbol{T}' \ , \tag{2.49}$$

where $(\cdot)^+$ denotes $\max(\cdot, 0)$. Equivalence with (2.13) is obvious.

For more about implicit constitutive theory, see articles [37], [38].

2.2.1 Construction of solution

We are solving the following problem

$$-\operatorname{div}\boldsymbol{T}' = \boldsymbol{b}, \qquad \boldsymbol{G}(\boldsymbol{T}', \boldsymbol{D}) = 0 \tag{2.50}$$

with response as in (2.49). For simplicity of solution construction, $\boldsymbol{u} = 0$ on $\partial\Omega$.

A couple $(\boldsymbol{T}', \boldsymbol{u}) \in L^2(\Omega)^{d\times d}_{sym} \times W^{1,2}_0(\Omega)^d$ is a weak solution to (2.50) if and only if

$$\int_\Omega \boldsymbol{T}' \cdot \boldsymbol{D}(\boldsymbol{u})\mathrm{d}x = \int_\Omega \boldsymbol{b}\cdot\boldsymbol{u}\mathrm{d}x \qquad \text{for all } \boldsymbol{u} \in W^{1,2}_0(\Omega)^d \ . \tag{2.51}$$

In this section we would like to outline a different approach how to prove an existence of the solution. More details and much broader scope as well as all the proofs can be found in [11], [12]. Many arguments from [10] are presented.

At first we introduce the graph $\mathcal{A} \subset \mathbb{R}^{d\times d}_{sym} \times \mathbb{R}^{d\times d}_{sym}$ by identifying with $\boldsymbol{G}$.

$$(\boldsymbol{T}', \boldsymbol{D}) \in \mathcal{A} \iff \boldsymbol{G}(\boldsymbol{T}', \boldsymbol{D}) \tag{2.52}$$

and we require fulfilling of the following assumptions

$$(0, 0) \in \mathcal{A} \ , \tag{2.53}$$

$$(\boldsymbol{T}_1' - \boldsymbol{T}_2') \cdot (\boldsymbol{D}_1 - \boldsymbol{D}_2) \geq 0 \quad \text{for all } (\boldsymbol{T}_1', \boldsymbol{D}),\ (\boldsymbol{T}_2', \boldsymbol{D}) \in \mathcal{A} \ , \tag{2.54}$$

$$\text{if } \big(\bar{\boldsymbol{T}}' - \boldsymbol{T}'\big) \cdot \big(\bar{\boldsymbol{D}} - \boldsymbol{D}\big) \geq 0 \quad \text{for all } \big(\bar{\boldsymbol{T}}', \bar{\boldsymbol{D}}\big) \in \mathcal{A} \text{ then } \big(\boldsymbol{T}', \boldsymbol{D}\big) \in \mathcal{A} \ , \tag{2.55}$$

there are positive c_*, d_* and an N-function ψ such that

$$\boldsymbol{T}' \cdot \boldsymbol{D} \geq c_* \left(\psi(\boldsymbol{D}) + \psi^*(\boldsymbol{T}')\right) - d_* \quad \text{for all } (\boldsymbol{T}', \boldsymbol{D}) \in \mathcal{A} \ . \tag{2.56}$$

ψ is an N-function if ψ is an even continuous convex function such that

$$\lim_{|s| \to 0+} \frac{\psi(s)}{|s|} = 0 \quad \text{and} \quad \lim_{|s| \to \infty} \frac{\psi(s)}{|s|} = \infty \ . \tag{2.57}$$

ψ^* is defined as the Legendre transform

$$\psi^*(s) := \sup_{l \in \mathbb{R}} (s \cdot l - \psi(l)) \ . \tag{2.58}$$

Let us have (2.49) in the form

$$\boldsymbol{D} = \frac{1}{2\eta} \frac{\boldsymbol{T}'(|\boldsymbol{T}'| - g)^+}{|\boldsymbol{T}'|} \tag{2.59}$$

The assumption (2.53) obviously holds.
Monotonicity (2.54) is satisfied as well, because $\frac{1}{2\eta}\frac{\boldsymbol{T}'(|\boldsymbol{T}'|-g)^+}{|\boldsymbol{T}'|}$ is monotone.
Regarding the maximality we set $\bar{\boldsymbol{T}}' = \boldsymbol{T} + \delta \boldsymbol{B}$, where $\boldsymbol{B} \in \mathbb{R}^{d \times d}_{sym}$ arbitrary. We obtain

$$\frac{1}{2\eta} \delta \boldsymbol{B} \left(\frac{(\boldsymbol{T}' + \delta \boldsymbol{T}')(|\boldsymbol{T}' + \delta \boldsymbol{B}|)}{|\boldsymbol{T}' + \delta \boldsymbol{V}|} - \boldsymbol{D} \right) \ , \tag{2.60}$$

which after dividing by δ a then $\delta \to 0$ together with continuity of all expressions implies $(\boldsymbol{T}', \boldsymbol{D}) \in \mathcal{A}$.
(2.56) is fulfilled with $\psi(|\boldsymbol{D}|) = \frac{1}{2}|\boldsymbol{D}|^2$, $\psi^*(\boldsymbol{T}') = \frac{1}{2}|\boldsymbol{T}'|^2$ and with matching c_* and d_*.

Now let $\mathcal{A}$ satisfy (2.53)–(2.56) and

$$\boldsymbol{T}'^n \rightharpoonup \boldsymbol{T}' \qquad \text{weakly in } L^2(\Omega)^{d \times d}_{sym} \ , \tag{2.61}$$

$$\boldsymbol{D}^n \rightharpoonup \boldsymbol{D} \qquad \text{weakly in } L^2(\Omega)^{d \times d}_{sym} \ , \tag{2.62}$$

$$(\boldsymbol{T}'^n(\boldsymbol{x}), \boldsymbol{D}^n(\boldsymbol{x})) \in \mathcal{A} \qquad \text{for all } n \text{ and a.a. } \boldsymbol{x} \in \Omega \ , \tag{2.63}$$

$$\limsup_{n \to \infty} \int_\Omega \boldsymbol{T}'^n \cdot \boldsymbol{D}^n \mathrm{d}x \leq \int_\Omega \boldsymbol{T}' \cdot \boldsymbol{D} \mathrm{d}x \ . \tag{2.64}$$

Then $(\boldsymbol{T}'(\boldsymbol{x}), \boldsymbol{D}(\boldsymbol{x})) \in \mathcal{A}$ for a.a. $\boldsymbol{x} \in \Omega$. A proof can be found in all cited references [10], [11] and [12].

Further we define finite k-dimensional subspace of $W^{1,2}_0(\Omega)^d$ that satisfies $\lim_{k \to \infty} V^k$ is dense in $W^{1,2}_0(\Omega)^d$.

We introduce an approximation $(\boldsymbol{T}'^k, \boldsymbol{D}^k) \in L^2(\Omega)^{d \times d}_{sym} \times V^k$

$$\int_\Omega \boldsymbol{T}^k \cdot \boldsymbol{D}^k(\boldsymbol{v}) \mathrm{d}x = \int_\Omega \boldsymbol{b} \cdot \boldsymbol{v} \mathrm{d}x \qquad \text{for all } \boldsymbol{v} \in V^k \tag{2.65}$$

$$(\boldsymbol{T}'^k, \boldsymbol{D}^k) \in \mathcal{A} \qquad \text{a.e. in } \Omega \ . \tag{2.66}$$

Let $\boldsymbol{v} = \boldsymbol{u}^k$, then it follows from (2.53)

$$\int_\Omega \psi(\boldsymbol{D}(\boldsymbol{v}^k)) + \psi^*(\boldsymbol{S}^k) \mathrm{d}x \leq C(\boldsymbol{b}) \ . \tag{2.67}$$

We extract further convergent subsequences leading directly to $-\operatorname{div} \boldsymbol{T}' = \boldsymbol{b}$ in weak sense.

To get $(\boldsymbol{T}', \boldsymbol{D}) \in \mathcal{A}$ a.e. in Ω, we follow the same procedure following (2.61).

Chapter 3

Numerical simulations

3.1 Problem formulations

As N. J. Walkington with J. S. Howell in [23] we start with standard primal mixed formulation with velocity and pressure. Further we introduce stress tensor deviator as an extra unknown and finally we also add symmetric part of velocity gradient as an unknown.

3.1.1 Primal mixed formulation

Consider Stokes like system

$$\begin{aligned} -\operatorname{div}\boldsymbol{T} &= \boldsymbol{b} && (3.1)\\ \operatorname{div}\boldsymbol{u} &= 0 && (3.2)\\ \boldsymbol{T} &= -p\boldsymbol{I}+\boldsymbol{T}' = -p\boldsymbol{I}+\mathcal{A}(\boldsymbol{D}(\boldsymbol{u})) && (3.3)\end{aligned}$$

We seek $(\boldsymbol{u},p)\in\mathbb{U}\times\mathbb{P}$ satisfying

$$\int_\Omega (\mathcal{A}(\boldsymbol{D}(\boldsymbol{u})) : \boldsymbol{D}(\boldsymbol{v}) - p\operatorname{div}\boldsymbol{v}) = \int_\Omega \boldsymbol{b}\cdot\boldsymbol{v} + \int_{\Gamma_1}\boldsymbol{t}\cdot\boldsymbol{v}\ , \quad \forall \boldsymbol{v}\in\mathbb{U}\ , \tag{3.4}$$

$$\int_\Omega q\operatorname{div}\boldsymbol{u} = 0\ , \quad \forall q\in\mathbb{P}\ . \tag{3.5}$$

This is a saddle point problem in the form

$$\begin{bmatrix} \tilde{\mathcal{A}} & -\operatorname{div}^T \\ \operatorname{div} & 0 \end{bmatrix}\begin{bmatrix}\boldsymbol{u}\\ p\end{bmatrix} = \begin{bmatrix}\boldsymbol{b}+\gamma^T(\boldsymbol{t})\\ 0\end{bmatrix}\ . \tag{3.6}$$

where $\langle\operatorname{div}^T(p),\boldsymbol{u}\rangle = (p,\operatorname{div}(\boldsymbol{u}))$ is the dual operator and $\langle\gamma^T(\boldsymbol{t}),\boldsymbol{v}\rangle = (\boldsymbol{t},\gamma(\boldsymbol{v}))_{\Gamma_1}$ is the dual of the trace operator γ. $(\cdot,\cdot)$ is the $L^2(\Omega)$ inner product and $\langle\cdot,\cdot\rangle$ is the induced duality pairing.

3.1.2 Extended formulation

Let us introduce to the unknowns $\boldsymbol{u}$ and p an extra unknown $\boldsymbol{S}$ corresponding to the Cauchy stress tensor deviator $\boldsymbol{T'}$. Then we seek $(\boldsymbol{u},p,\boldsymbol{S})\in\mathbb{U}\times\mathbb{P}\times\mathbb{S}$ such that

$$\int_\Omega (\boldsymbol{S} : \boldsymbol{D}(\boldsymbol{v}) - p\operatorname{div}\boldsymbol{v}) = \int_\Omega \boldsymbol{b}\cdot\boldsymbol{v} + \int_{\Gamma_1}\boldsymbol{t}\cdot\boldsymbol{v}\ , \quad \forall \boldsymbol{v}\in\mathbb{U}\ , \tag{3.7}$$

$$\int_\Omega q \operatorname{div} \boldsymbol{u} = 0 \;, \quad \forall q \in \mathbb{P} \;, \tag{3.8}$$

$$\int_\Omega (\boldsymbol{S} - \mathcal{A}(\boldsymbol{D}(\boldsymbol{u}))) : \boldsymbol{T} = 0 \;, \quad \forall \boldsymbol{T} \in \mathbb{S} \;. \tag{3.9}$$

or in the form

$$\begin{bmatrix} 0 & -\operatorname{div}^T & \boldsymbol{D}^T(\cdot) \\ \operatorname{div} & 0 & 0 \\ \tilde{\mathcal{A}} & 0 & -\boldsymbol{I} \end{bmatrix} \begin{bmatrix} \boldsymbol{u} \\ p \\ \boldsymbol{S} \end{bmatrix} = \begin{bmatrix} \boldsymbol{b} + \gamma^T(\boldsymbol{t}) \\ 0 \\ 0 \end{bmatrix} \;, \tag{3.10}$$

where similarly to the previous dual operators $\langle \boldsymbol{D}^T(\boldsymbol{S}), \boldsymbol{u} \rangle = (\boldsymbol{S}, \boldsymbol{D}(\boldsymbol{u}))$.

With these equations one can already prescribe implicit constitutive equations in the form $\boldsymbol{G}(\boldsymbol{T}, \boldsymbol{D}) = 0$ replacing the term $\boldsymbol{S} - \mathcal{A}(\boldsymbol{D}(\boldsymbol{u}))$.

3.1.3 Dual mixed formulation

In addition to the previous formulation we add symmetric part of the velocity gradient $\boldsymbol{D}$ resulting in the full system of equations. Then $(\boldsymbol{u}, p, \boldsymbol{S}, \boldsymbol{D}) \in \mathbb{U} \times \mathbb{P} \times \mathbb{S} \times \mathbb{D}$ satisfies

$$\int_\Omega (\boldsymbol{S} : \boldsymbol{D}(\boldsymbol{v}) - p \operatorname{div} \boldsymbol{v}) = \int_\Omega \boldsymbol{b} \cdot \boldsymbol{v} + \int_{\Gamma_1} \boldsymbol{t} \cdot \boldsymbol{v} \;, \quad \forall \boldsymbol{v} \in \mathbb{U} \;, \tag{3.11}$$

$$\int_\Omega q \operatorname{div} \boldsymbol{u} = 0 \;, \quad \forall q \in \mathbb{P} \;, \tag{3.12}$$

$$\int_\Omega (\boldsymbol{S} - \mathcal{A}(\boldsymbol{D})) : \boldsymbol{T} = 0 \;, \quad \forall \boldsymbol{T} \in \mathbb{S} \;, \tag{3.13}$$

$$\int_\Omega (\boldsymbol{D} - \boldsymbol{D}(u)) : \boldsymbol{E} = 0 \;, \quad \forall \boldsymbol{E} \in \mathbb{D} \tag{3.14}$$

also written as

$$\begin{bmatrix} 0 & -\operatorname{div}^T & \boldsymbol{D}^T(\cdot) & 0 \\ \operatorname{div} & 0 & 0 & 0 \\ 0 & 0 & -\boldsymbol{I} & \tilde{\mathcal{A}} \\ \boldsymbol{D}(\cdot) & 0 & 0 & -\boldsymbol{I} \end{bmatrix} \begin{bmatrix} \boldsymbol{u} \\ p \\ \boldsymbol{S} \\ \boldsymbol{D} \end{bmatrix} = \begin{bmatrix} \boldsymbol{b} + \gamma^T(\boldsymbol{t}) \\ 0 \\ 0 \\ 0 \end{bmatrix} \;. \tag{3.15}$$

In the discrete version of the last formulation spaces $\mathbb{S}_h$ and $\mathbb{D}_h$ coincide, hence (3.15) is basically the same as “Alternative dual mixed formulation” with pressure in [23].

3.2 Used FEM software

All simulations were carried out using FEM software developed by Jaroslav Hron. Software description can be partially found in [24] and [17]. Let us just mention basic principles this computation code builds on. We omit time discretization, since all the problems covered in the text are stationary.

The discretization in space, as already mentioned, is done by finite element method. The considered domain Ω is approximated by the polygonal domain Ω_h covered with quadrilaterals $\mathcal{T}_h$. Any two quadrilaterals are disjoint or have a common node or edge.

Let us consider primal mixed formulation, i.e. equations (3.4)–(3.5), which take following discrete form

$$\int_\Omega (\mathcal{A}(\boldsymbol{D}(\boldsymbol{u}_h)) : \boldsymbol{D}(\boldsymbol{v}) - p_h \operatorname{div} \boldsymbol{v} + q \operatorname{div} \boldsymbol{u_h}) = \\ = \int_\Omega \boldsymbol{f} \cdot \boldsymbol{v} + \int_{\Gamma_1} \boldsymbol{t} \cdot \boldsymbol{v} \ , \qquad \forall (\boldsymbol{v}, q) \in \mathbb{U}_h \times \mathbb{P}_h \tag{3.16}$$

We denote $\{v^i\}$ a basis for $\mathbb{V}_h$ and $\{q^i\}$ a basis for $\mathbb{P}_h$, then

$$\boldsymbol{u}_h = \sum U_i v^i \ , \tag{3.17}$$

$$\boldsymbol{p}_h = \sum P_i q^i \ . \tag{3.18}$$

Denoting $\boldsymbol{X} = (U, P)$, the finite dimensional nonlinear system is

$$\mathcal{F}(\boldsymbol{X}) = \boldsymbol{0} \ . \tag{3.19}$$

Such system of nonlinear algebraic equations is solved using Newton method. One iteration step is given by

$$\boldsymbol{X}^{n+1} = \boldsymbol{X}^n - \left[\frac{\partial \mathcal{F}}{\partial \boldsymbol{X}} (\boldsymbol{X}^n)\right]^{-1} \mathcal{F}(\boldsymbol{X}^n) \ . \tag{3.20}$$

These iterations converge quadratically for $\|\boldsymbol{X} - \boldsymbol{X}^0\|$ small. To ensure global convergence, solution update step is replaced by

$$\boldsymbol{X}^{n+1} = \boldsymbol{X}^n + \omega \delta \boldsymbol{X} \ , \quad \omega \in [-1, 0) \ . \tag{3.21}$$

The Jacobian is computed by finite differences from the residual vector $\mathcal{F}(\boldsymbol{X})$

$$\left[\frac{\partial \mathcal{F}}{\partial \boldsymbol{X}}\right]_{ij} (\boldsymbol{X}^n) \approx \frac{[\mathcal{F}]_i(\boldsymbol{X}^n + \alpha_j e_j) - [\mathcal{F}]_i(\boldsymbol{X}^n - \alpha_j e_j)}{2\alpha_j} \ , \tag{3.22}$$

where e_j are unit basis vectors in $\mathbb{R}^n$ and α_j are coefficients generally iteration-dependent.

A direct sparse solver `UMFPACK` has always been used for matrix inversion.

Finally we address the choice of finite element spaces. For the primal mixed formulation we use Q_2/P_1^{disc} element pair satisfying Ladyzhenskaya-Babuška-Brezzi condition, see [26].

Analogically we would derive discrete versions of both other formulations with interpolation to spaces $\mathbb{S}_h$ and $\mathbb{D}_h$. Retracing and considering Bingham fluid for the approach in [21], [6], [5], [4] or [7], these spaces must comply with following points.

The velocity-pressure interpolation must satisfy the usual LBB condition. Both continuous and discontinuous interpolation may be used for extra stress tensor. If a discontinuous interpolations of the extra stress tensor $\boldsymbol{S}$ is used, the space of the symmetric part of the velocity gradient $\boldsymbol{D}$ as obtained after differentiation of the velocity field $\boldsymbol{u}$ must be included in the interpolation space of the extra stress tensor $\boldsymbol{S}$, i.e. $\mathbb{D} \subset \mathbb{S}$.

Meeting the criteria above, we consider either Q_2 or Q_{2*}^{disc} elements for extra stress and the same space for the symmetric part of the velocity gradient.

The finite dimensional spaces are as follows

$$\mathbb{U}_h = \left\{\boldsymbol{u}_h \in [H_0^1(\Omega_h)]^2 | \boldsymbol{u}_{h|T} \in [Q_2(T)]^2 \quad \forall T \in \mathcal{T}_h\right\} \ , \tag{3.23}$$

$$\mathbb{P}_h = \left\{p_h \in L^2(\Omega_h) | p_{h|T} \in P_1(T) \quad \forall T \in \mathcal{T}_h\right\} \ , \tag{3.24}$$

$$\mathbb{S}_h = \mathbb{D}_h = \left\{ \boldsymbol{x}_h \in [H_0^1(\Omega_h)]^4 | \boldsymbol{x}_{h|T} \in [Q_2(T)]^4 \quad \forall T \in \mathcal{T}_h \right\} \ , \tag{3.25}$$

or

$$\mathbb{S}_h = \mathbb{D}_h = \left\{ \boldsymbol{x}_h \in [L^2(\Omega_h)]^4 | \boldsymbol{x}_{h|T} \in [Q_{2*}(T)]^4 \quad \forall T \in \mathcal{T}_h \right\} \ . \tag{3.26}$$

Consider $\forall T \in \mathcal{T}_h$ bilinear transformation $\psi_T : \hat{T} \to T$ from the reference element $\hat{T}$ to the unit square T. Then

$$Q_2(T) = \left\{ q \circ \psi_T^{-1} | q \in \operatorname{span}\langle 1, x, y, xy, x^2, y^2, x^2y, xy^2, x^2y^2 \rangle \right\} \ . \tag{3.27}$$

Local degrees of freedom are located at the nodes, edges' midpoints and center of T.

$$P_1(T) = \left\{ q \circ \psi_T^{-1} | q \in \operatorname{span}\langle 1, x, y \rangle \right\} \tag{3.28}$$

with value and both partial derivatives located in the center of T.

$$Q_{2*}(T) = \left\{ q \circ \psi_T^{-1} | q \in \operatorname{span}\langle 1, x, y, xy, x^2, y^2, x^2y, xy^2 \rangle \right\} \ , \tag{3.29}$$

value and all derivatives are again located in the center of T.

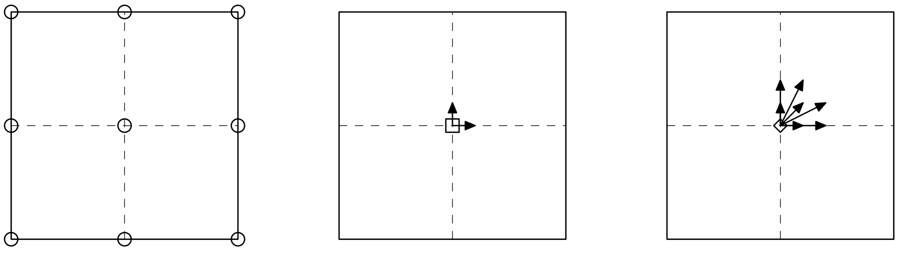
(a) Q_2 (b) P_1 (c) Q_{2*}

Figure 3.1: Location of degrees of freedom

3.3 Governing equations

All computed problems are considered as stationary, isothermal flows with small inertia. Such model reduction leaves us with governing equations

$$\operatorname{div} \boldsymbol{T}' - \nabla p = 0 \ , \tag{3.30}$$

$$\operatorname{div} \boldsymbol{u} = 0 \ . \tag{3.31}$$

For constitutive relation $\boldsymbol{G}(\boldsymbol{T}, \boldsymbol{D})$ we considered two options. The first one is a regularized version of a classical constitutive equation as in section 2.1.3, i.e.

$$\boldsymbol{T}' |\boldsymbol{D}_\varepsilon| - 2\eta \boldsymbol{D} |\boldsymbol{D}_\varepsilon| + g\boldsymbol{D} = 0 \ , \tag{3.32}$$

where $|\boldsymbol{D}_\varepsilon| = \sqrt{|\boldsymbol{D}|^2 + \varepsilon^2}$. The other one is a modified relation from section 2.2.

$$2\eta \boldsymbol{D} \left(g + \left(|\boldsymbol{T}'| - g \right)_\varepsilon^+ \right) = \left(|\boldsymbol{T}'| - g \right)_\varepsilon^+ \boldsymbol{T}' \ , \tag{3.33}$$

where $(\cdot)_\varepsilon^+$ denotes $\max(\cdot, \varepsilon)$.

$|\boldsymbol{D}(\boldsymbol{u})|$ is a Frobenius norm of tensor $\boldsymbol{D}(\boldsymbol{u})$, meaning

$$|\boldsymbol{D}(\boldsymbol{u})| = \left(\sum_{1 \le i,j \le 2} |D_{ij}(\boldsymbol{u})|^2 \right)^{1/2} \ . \tag{3.34}$$

This choice of norm (same as in [18]) requires scaling factor of $\sqrt{2}$ for yield stress to keep same dimensionless characteristics as for example in [47] or others with the same choice of norm.

Velocity components are denoted u and v, i.e

$$\boldsymbol{u} = (u, v) \ . \tag{3.35}$$

3.4 Poiseuille flow

The problem of the creeping flow of a viscoplastic material under the a pressure gradient is schematically shown in Fig. 3.2. The governing equations remains (3.30)–(3.34).

Constitutive equation (3.32) is labeled for use in graphs and tables as `T`, while equation (3.33) is labeled as `D`.

Prescribed boundary conditions are as follows. For the y-component v of velocity, we set homogeneous Dirichlet boundary condition on the whole boundary. For the x-component u of velocity, we prescribe homogeneous Dirichlet boundary condition on the plates and Neumann boundary conditions on the inlet and outlet.

$$\boldsymbol{u} = 0 \qquad \text{on } \Gamma_2 \ , \tag{3.36}$$

$$\boldsymbol{t}_n^* = 0 \ , \ v = 0 \qquad \text{on } \Gamma_1 \ , \tag{3.37}$$

$$\boldsymbol{t}_n^* = -32 \ , \ v = 0 \qquad \text{on } \Gamma_3 \ . \tag{3.38}$$

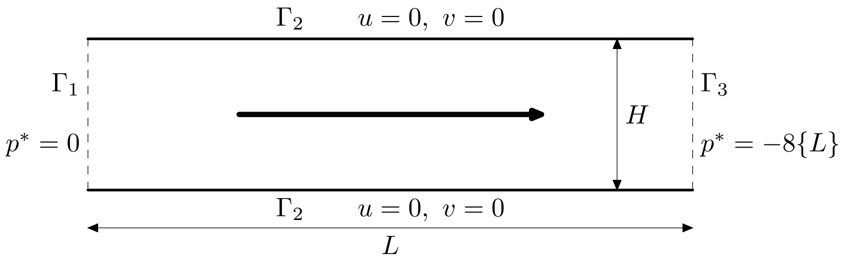

Figure 3.2: Schematic representation of boundary conditions

As for the analytical solution to the problem,

$$Y = \frac{g}{\sqrt{2}} \frac{1}{\frac{\mathrm{dp}}{\mathrm{d}} x} \ , \tag{3.39}$$

Y denotes the distance of yield surface from the channel midpoint $H/2$. Then

$$u = \frac{1}{2\eta} \frac{\mathrm{dp}}{\mathrm{dx}} y(H - y) - \frac{g}{\sqrt{2}} \frac{1}{\eta} y \ , \quad 0 \le y \le \frac{H}{2} - Y \tag{3.40}$$

and

$$u = \frac{1}{2\eta} \frac{\mathrm{dp}}{\mathrm{dx}} y(H - y) - \frac{g}{\sqrt{2}} \frac{1}{\eta} (H - y) \ , \quad \frac{H}{2} + Y \le y \le H \ . \tag{3.41}$$

The solution in the middle part of the channel is constant, and continuous,

$$u = u(H/2 - Y) = u(H/2 + Y) \ , \quad \frac{H}{2} - Y \le y \le \frac{H}{2} + Y \ , \tag{3.42}$$

where values $u(H/2 - Y)$ and $u(H/2 + Y)$ are given by (3.40) and (3.41). Velocity component v is zero and pressure distribution is linear along the channel.

Following results are given in dimensionless quantities. Lengths are scaled with corresponding channel dimension. All velocities with U_N, which is a maximal velocity of Newtonian fluid under the same conditions, pressure and stress with $\eta U_N/H$

$$x^* = \frac{x}{L} \ , \qquad y^* = \frac{x}{H} \ , \qquad u^* = \frac{u}{U_N} \ , \qquad p^* = \frac{pH}{\eta U_N} \ . \tag{3.43}$$

It is appropriate to introduce dimensionless yield stress and dimensionless Bingham number Bn, for example as in [2]

$$g^* = \frac{\sqrt{2}gH}{\eta U_N} \ , \qquad Bn = \frac{\sqrt{2}gH}{\eta U_B} \ , \tag{3.44}$$

where U_B is a maximal velocity of flow with corresponding yield stress g. Newtonian fluid corresponds to $Bn = 0$, while an unyielded solid to $Bn \to \infty$ or g^* reaches dimensionless pressure gradient defined by

$$\Delta p^* = \frac{\mathrm{d}p}{\mathrm{d}x}\frac{H^2}{\eta U_N} \ . \tag{3.45}$$

In the first part we would like to present the results of a thorough testing of different formulations, different elements for added unknowns and also different constitutive equations. We have to say that $\boldsymbol{u}$-p (primal mixed) fomrulation is omitted. The reason is that we were unable to converge to the the satisfying results for yield stresses higher than insignificant. All remaining 8 combinations were tested in more than 200 simulations of Poiseuille flow.

Meshes were always divided into 4 cells along the channel and into 16–512 cells across the channel. An example of the mesh with 64 cells in total is in Fig. 3.3. Δp^* was set to 8.0. Simulations covered the whole range $0 \leq Bn < \infty$.

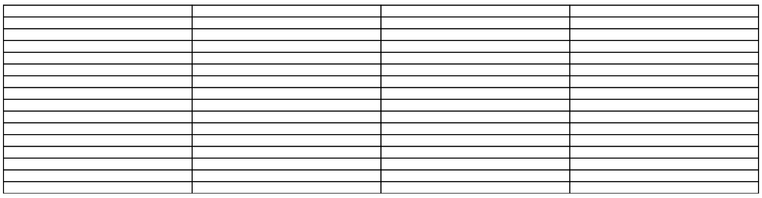

Figure 3.3: Example of used mesh, $h = 1/16$

Computations usually starts with high regularization parameter ε and then continues with one or more following iterations, when ε is taken down to the values close to zero. An iteration always takes previous result as an initial solution vector for Newton method. The stepping is heavily dependent on the problem, mesh, elements and used formulation.

For the yield stress $Bn = 10.3$ ($g^* = 3.4$), different approaches were compared in terms of maximal velocity achieved and the width of unyielded region. As a criterion to determine whether a region is unyielded or not, a $|\boldsymbol{D}| < 0.001$ as in [35] was chosen .The results are presented in Tab. 3.1, 3.2 and corresponding visualisations in Fig. 3.4, 3.5.

In addition simple convergence tests we carried. For the same yield stress on the different meshes we set regularization parameter ε to the certain value and start the simulation with the flow of Newtonian fluid as the initial solution vector without any other ε iterations. Lowest achieved εs are in Tab. 3.3 and in Fig. 3.6. Actual numbers of nonlinear iterations are in the last part of the thesis as an attachments.

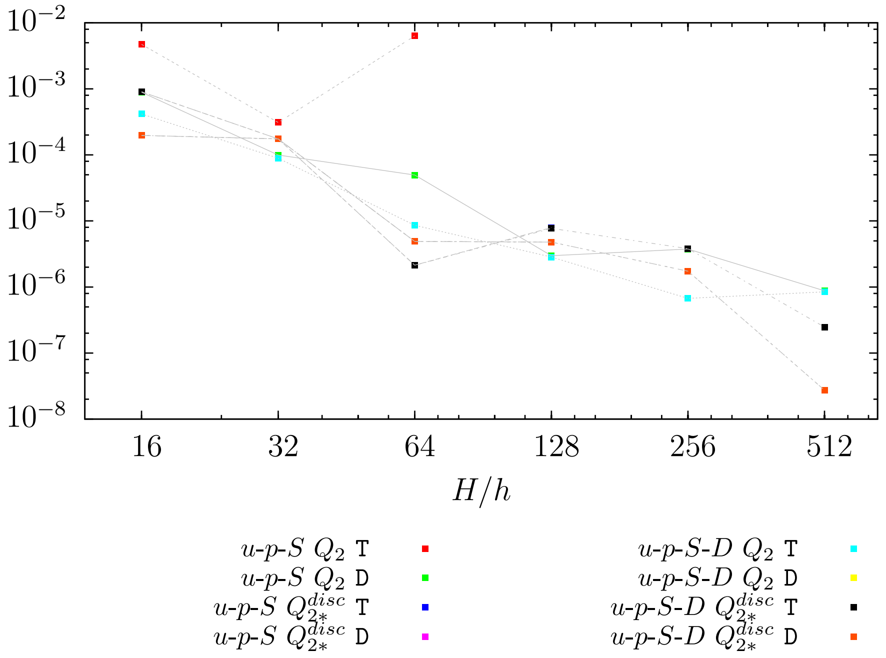

Figure 3.4: u_{max} error for Poiseuille flow with $Bn = 10.3$ ($g^* = 3.4$)

		const.				H/h		
formulation	$\boldsymbol{S}$, $\boldsymbol{D}$ el.	eq.	16	32	64	128	256	512
$\boldsymbol{u}$-p-$\boldsymbol{S}$	Q_2	T	4.73e-3	3.10e-4	6.35e-3	$^{1)}$	$^{1)}$	$^{1)}$
		D	8.96e-4	1.00e-4	4.97e-5	2.98e-6	3.76e-6	8.72e-6
	$\mathrm{Q}_{2*}^{\mathrm{disc}}$	T	9.04e-4	1.75e-4	2.14e-6	7.94e-6	$^{1)}$	$^{1)}$
		D	1.98e-4	1.75e-4	4.90e-6	4.79e-6	1.73e-6	2.74e-8
$\boldsymbol{u}$-p-$\boldsymbol{S}$-$\boldsymbol{D}$	Q_2	T	4.17e-4	8.88e-5	8.56e-6	2.84e-6	6.73e-7	8.48e-7
		D	1.98e-4	1.75e-4	4.90e-6	4.79e-6	$^{2)}$	$^{2)}$
	$\mathrm{Q}_{2*}^{\mathrm{disc}}$	T	9.04e-4	1.75e-4	2.14e-6	7.94e-6	3.81e-6	2.47e-7
		D	1.98e-4	1.75e-4	4.90e-6	4.79e-6	1.73e-6	2.74e-8

Table 3.1: u^*_{max} error for Poiseuille flow with $Bn = 10.3$ ($g^* = 3.4$)
$^{1)}$ did not converge, $^{2)}$ ran out of memory during matrix inversion

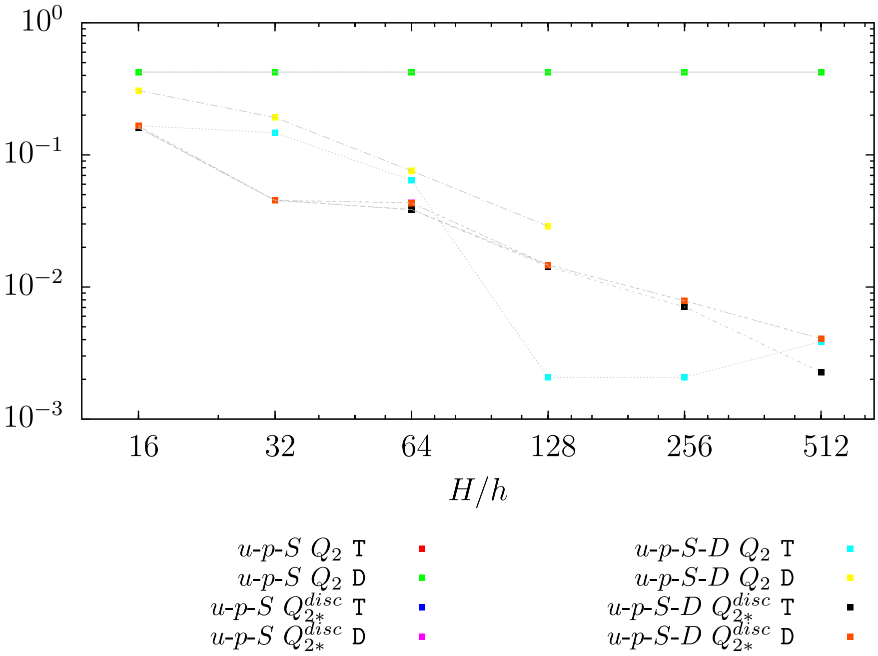

Figure 3.5: Unyielded region width error for Poiseuille flow with $Bn = 10.3$ ($g^* = 3.4$)

		const.	H/h					
formulation	$\boldsymbol{S}$, $\boldsymbol{D}$ el.	eq.	16	32	64	128	256	512
$\boldsymbol{u}$-p-$\boldsymbol{S}$	Q_2	T	4.24e-1	4.24e-1	4.24e-1	1)	1)	1)
		D	4.24e-1	4.24e-1	4.24e-1	4.24e-1	4.24e-1	4.24e-1
	Q_{2*}^{disc}	T	1.60e-1	4.53e-2	3.87e-2	1.47e-2	1)	1)
		D	1.66e-1	4.53e-2	4.35e-2	1.47e-2	7.86e-3	4.06e-3
$\boldsymbol{u}$-p-$\boldsymbol{S}$-$\boldsymbol{D}$	Q_2	T	1.66e-1	1.47e-1	6.43e-2	2.06e-3	2.06e-3	3.87e-3
		D	3.07e-1	1.92e-1	7.57e-2	2.89e-2	2)	2)
	Q_{2*}^{disc}	T	1.60e-1	4.53e-2	3.85e-2	1.43e-2	7.06e-3	2.26e-3
		D	1.66e-1	4.53e-2	4.33e-2	1.47e-2	7.86e-3	4.06e-3

Table 3.2: Unyielded region width error for Poiseuille flow with $Bn = 10.3$ ($g^* = 3.4$)
1) did not converge, 2) ran out of memory during matrix inversion

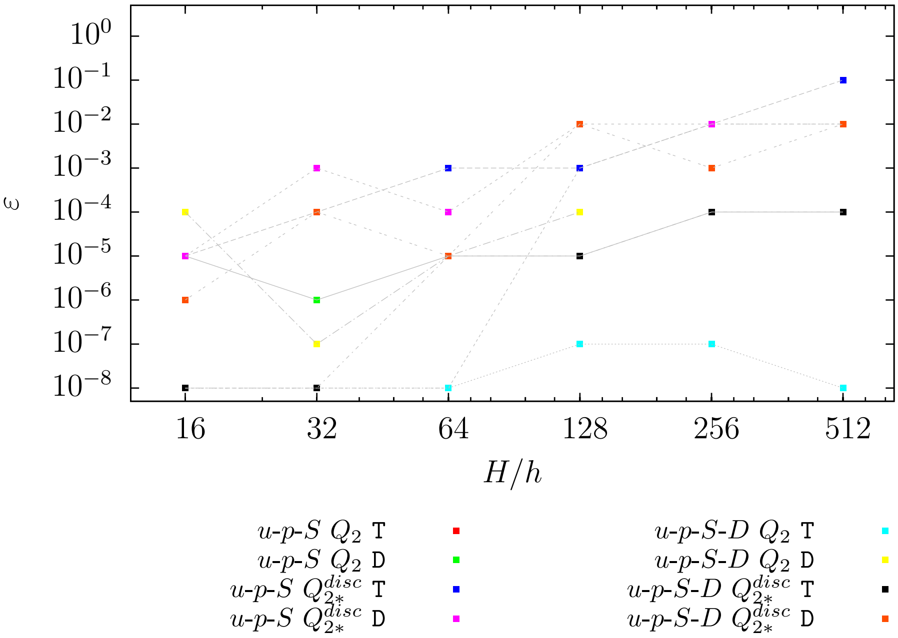

Figure 3.6: ε achieved without any regularization stepping starting from solution for $\varepsilon \to \infty$, Poiseuille flow with $Bn = 10.3$
($g^* = 3.4$)

		const.	H/h					
formulation	$\boldsymbol{S}$, $\boldsymbol{D}$ el.	eq.	16	32	64	128	256	512
$\boldsymbol{u}$-p-$\boldsymbol{S}$	Q_2	`T`	1e-8	1e-8	1e-8	1e-3	1e-2	1e-2
		`D`	1e-5	1e-6	1e-5	1e-5	1e-4	1e-4
	$\mathrm{Q}_{2*}^{\mathrm{disc}}$	`T`	1e-5	1e-4	1e-3	1e-3	1e-2	1e-1
		`D`	1e-5	1e-3	1e-4	1e-2	1e-2	1e-2
$\boldsymbol{u}$-p-$\boldsymbol{S}$-$\boldsymbol{D}$	Q_2	`T`	1e-8	1e-8	1e-8	1e-7	1e-7	1e-8
		`D`	1e-4	1e-7	1e-5	1e-4	1)	1)
	$\mathrm{Q}_{2*}^{\mathrm{disc}}$	`T`	1e-8	1e-8	1e-5	1e-5	1e-4	1e-4
		`D`	1e-6	1e-4	1e-5	1e-2	1e-3	1e-2

Table 3.3: ε achieved without any regularization stepping starting from solution for $\varepsilon \to \infty$, Poiseuille flow with $Bn = 10.3$
($g^* = 3.4$)

Considering previous data from comparison we conclude the following chart

	$\boldsymbol{u}$-p-$\boldsymbol{S}$				$\boldsymbol{u}$-p-$\boldsymbol{S}$-$\boldsymbol{D}$			
	Q_2		Q_{2*}^{disc}		Q_2		Q_{2*}^{disc}	
criteria	`T`	`D`	`T`	`D`	`T`	`D`	`T`	`D`
precision	✖	✖	✖	✔	✔	✖	✔	✔
convergence	✖	✔	✖	▬	✔	✖	✔	▬

Table 3.4: Comparison conclusion chart

The Tab. 3.4 shows:

- Adding $\boldsymbol{D}$ as an extra unknown has two different effects
  - if it is interpolated into continuous space, then it will improve accuracy heavily, especially in regions with low $|\boldsymbol{D}|$
  - it improves convergence of Newton method independently of used elements, the problem is more coupled
- Usage of classical regularized formulation (3.32) requires $\boldsymbol{u}$-p-$\boldsymbol{S}$-$\boldsymbol{D}$ formulation as it helps with the problematic term $|\boldsymbol{D}|$
- Usage of classical regularized formulation (3.32) allows us to use both continuous and discontinuous elements for extra stress and velocity gradient
- Usage of regularized formulation from implicit equation (3.33) with continuous elements for extra stress and velocity gradient carries higher memory requirements for matrix inversion, hence discontinuous elements for extra stress and velocity gradient are advised
- Usage of regularized formulation from implicit equation (3.33) converges in only a few iterations, making it very fast, but on the other hand it requires fine stepping in ε iterations

Further we focus mainly on $\boldsymbol{u}$-p-$\boldsymbol{S}$-$\boldsymbol{D}$ formulation with discontinuous elements for extra stress and velocity gradient. This combination allows us to use both constitutive equations, achieves high precision and is reliable.

Other suitable combinations are:

1. $\boldsymbol{u}$-p-$\boldsymbol{S}$, with discontinuous elements for extra stress and velocity gradient with constitutive equation (3.33). As mentioned earlier there is no difference in precision in comparison with $\boldsymbol{u}$-p-$\boldsymbol{S}$-$\boldsymbol{D}$ formulation, however such combination requires even finer ε-stepping in comparison to the preferred combination.
2. $\boldsymbol{u}$-p-$\boldsymbol{S}$-$\boldsymbol{D}$ with continuous elements for extra stress and velocity gradient with constitutive equation (3.32). Such combination is similar to the preferred one both in terms of precision and convergence. It might even seem like that this combination is superior considering convergence test, but additional tests in more complicated geometries reveals that both are comparable and on par. Continuous elements carry less degrees of freedom, but the matrix inversion during each step of Newton iterations are more memory and CPU time demanding.

Finally we present results for $\boldsymbol{u}$-p-$\boldsymbol{S}$-$\boldsymbol{D}$ formulation with discontinuous elements for extra stress and symmetric part of velocity gradient and (3.32) constitutive equation on the finest mesh $H/h = 512$, i.e. 2048 elements in total.

Growth of the unyielded region is in Fig. 3.7, linear pressure distribution is shown in Fig. 3.8 and several velocity profiles are in Fig. 3.9.

Last figures 3.10 and 3.11 pictures dependency of previously studied u^*_{max} and width of the plug on the Bingham number Bn and yield stress g^*.

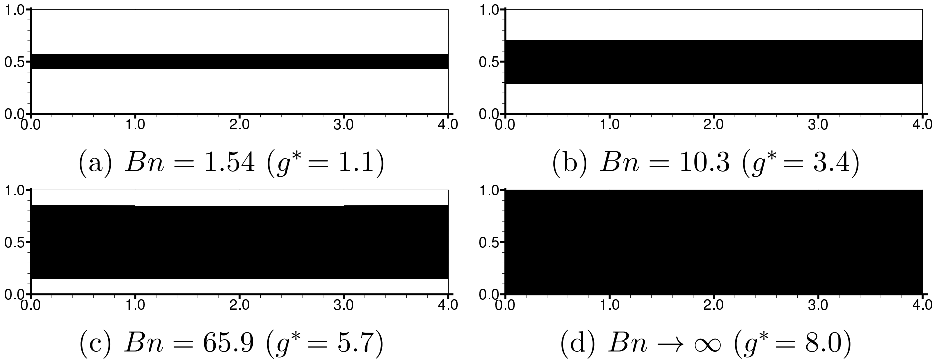

(a) $Bn = 1.54$ ($g^* = 1.1$)

(b) $Bn = 10.3$ ($g^* = 3.4$)

(c) $Bn = 65.9$ ($g^* = 5.7$)

(d) $Bn \to \infty$ ($g^* = 8.0$)

Figure 3.7: Unyielded region for different yield stresses

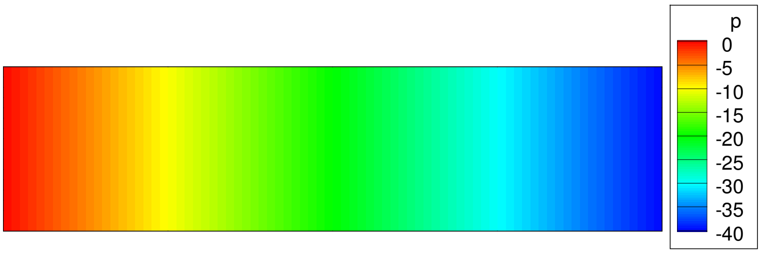

Figure 3.8: Pressure distribution along the channel

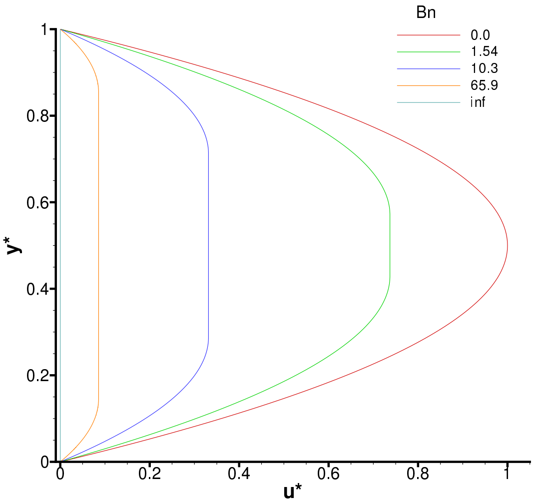

Figure 3.9: Computed velocity profiles across the channel

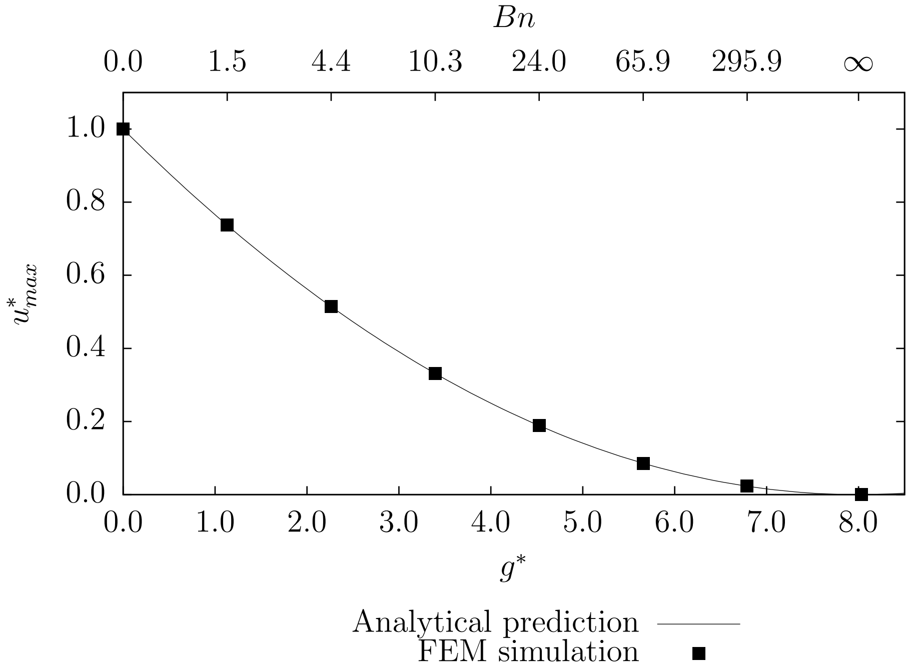

Figure 3.10: Maximal velocities for different yield stresses

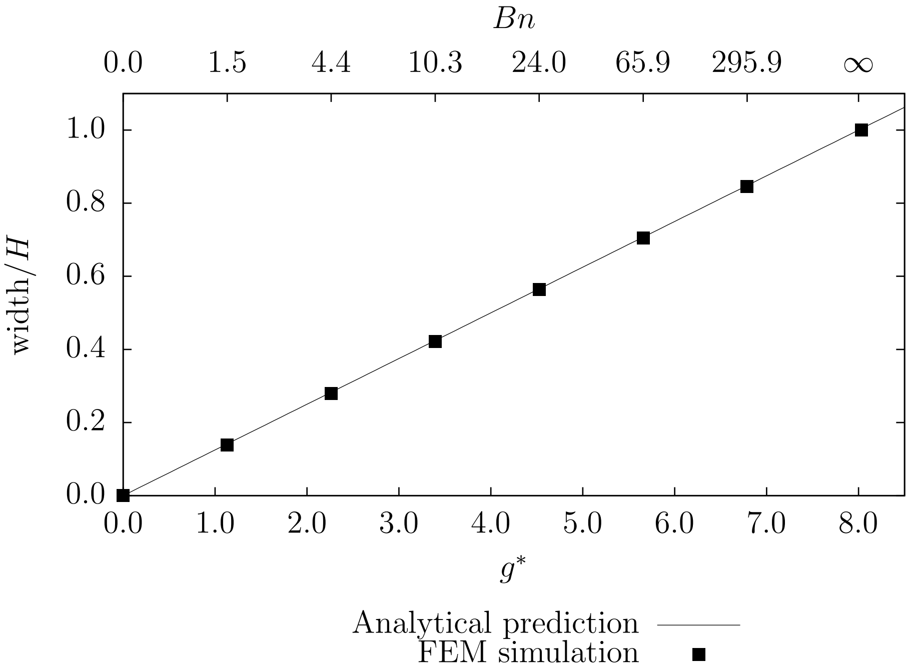

Figure 3.11: Unyielded region width for different yield stresses

3.5 Lid-driven cavity

In this section we would like to present our results of typical benchmark simulation. As mentioned in the first chapter, this problem has already been studied, beginning with [8] in 1980, and published recently in [34] from 2009 and 2011 preprint [3]. All these simulations were carried in range of Bingham number 0–10. The only article that came to our knowledge presenting simulations going a way further is [30] with Bingham number up to 100,000.

We introduce Bingham number

$$Bn = \frac{\sqrt{2} g H}{\eta U} \ , \tag{3.46}$$

where $\sqrt{2}$ results from the used norm. Characteristic dimension H (width and height of the domain), velocity U (velocity of the lid) and viscosity η are set as unity.

Our problem setting is the same as in [47] using previously described methods and formulations. The governing equations are (3.30)–(3.34).

Boundary conditions are in Fig. 3.12. As it can be seen, tangential velocity on the top boundary is not regularized, instead an interpolation on the side boundaries by the top corners guarantees that the velocity is continuous. This also means that there is an inflow/outflow through the left/right boundary nearby the top corners.

$$u^* = 1 \qquad \text{on } \Gamma_2 \ , \tag{3.47}$$

$$u^* = 0 \qquad \text{on } \Gamma_1 \setminus \epsilon \ , \tag{3.48}$$

$$v^* = 0 \qquad \text{on } \Gamma_1 \cup \Gamma_2 \ . \tag{3.49}$$

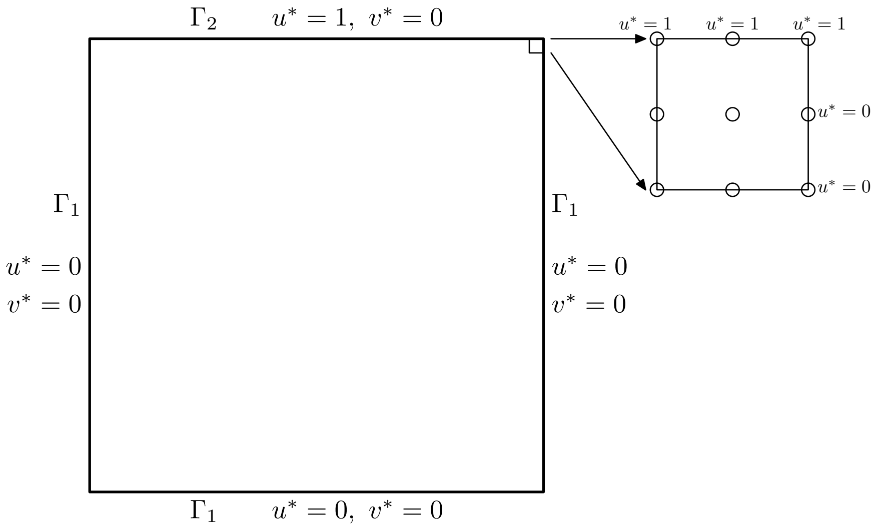

Figure 3.12: Boundary conditions

Whole range of $0 \leq Bn \leq 100,000$ has been studied. Both regularized versions of constitutive relations were applied and the results were basically the same. Since convergence and iterating over regularization coefficient ε was easier with (3.32), all the presend results are achieved with this constitutive relation. Used mesh consists of 1024 same elements in 32×32 grid, see Fig. 3.13.

The unyielded region grows as the Bingham number increases. Such behaviour has been reported in all cited related articles. One possible criterion for visualisation of

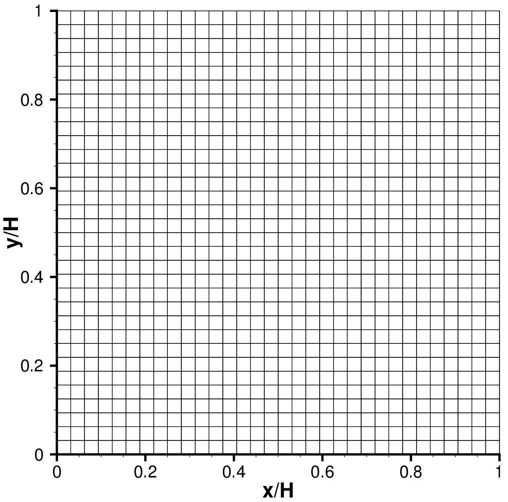

Figure 3.13: Used mesh, 32 × 32 elements

unyielded regions is Von Mises condition (2.5), this approach is supposed to be more precise an relies only on variables directly connected with the problem. However we have encountered a problem with zig-zag behaviour as mentioned in [30], [29] or [47]. The other possibility is to mark area, where $|\boldsymbol{D}| < \epsilon$ as we did in previous section. Remaining question is how to determine a correct value of ϵ, too low values lead to underestimation of the unyielded area and vice versa. Our method combines both of these approaches. Firstly we start with the Von Mises criterion and then for the final form of figure, we set the ϵ to match the Von Mises criterion, but without zig-zag artifacts. For the lid-driven cavity, the ϵ value has been set as 0.005, i.e. gray area in Fig. 3.14 represents $|\boldsymbol{D}| < 0.005$. These results are, given the figures comparison, similar to those presented in [30]. We see the main difference in the shape of the upper unyielded region, the lower unyielded regions exhibits basically the previously reported size and shape.

Except the unyielded regions, also the pressure along the lid, vortex intensity and eye of the vortex position were computed in [30]. Our results are in Fig. 3.15–3.17. Regarding the pressure, our computed values are nearby the corners about 25–35% lower, further improvement of these values would require finer mesh. The vortex intensity (value of the stream function in the eye of the vortex) is in accordance with [30] for the $Bn \approx O(10^2)$, further Mitsoulis and Zisis calculated almost stable vortex intensity, we have observed alike behaviour for $Bn \approx O(10^4)$, about 10-times higher. Vortex center lies from the symmetry at $x/H = 0.5$, the vertical coordinate y/H vs. Bingham number is in Fig. 3.17. General shape of the curve agrees with the one in the article, the values for $Bn = 0$ and $Bn > 1000$ differs by less than 1%. However in the middle area finer mesh would certainly improve the results.

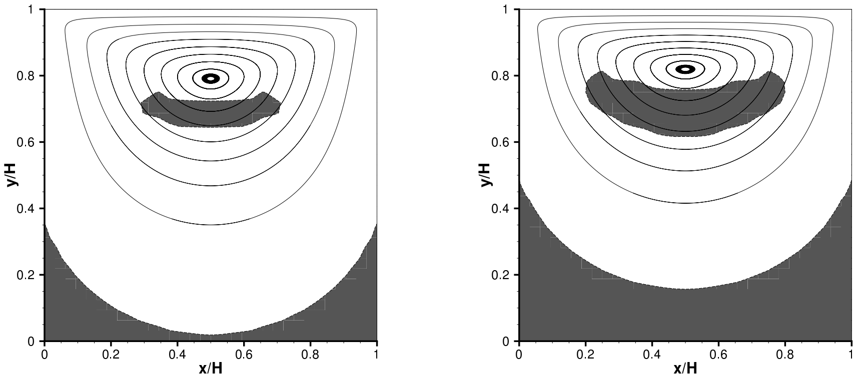

(a) $Bn = 2.0$ (b) $Bn = 5.0$

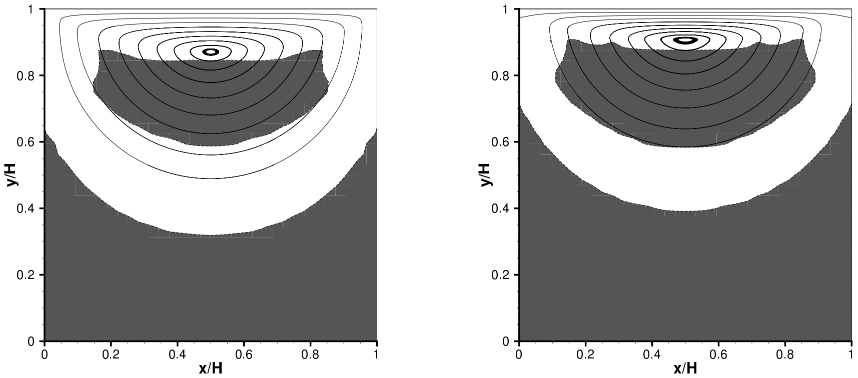

(c) $Bn = 20.0$ (d) $Bn = 50.0$

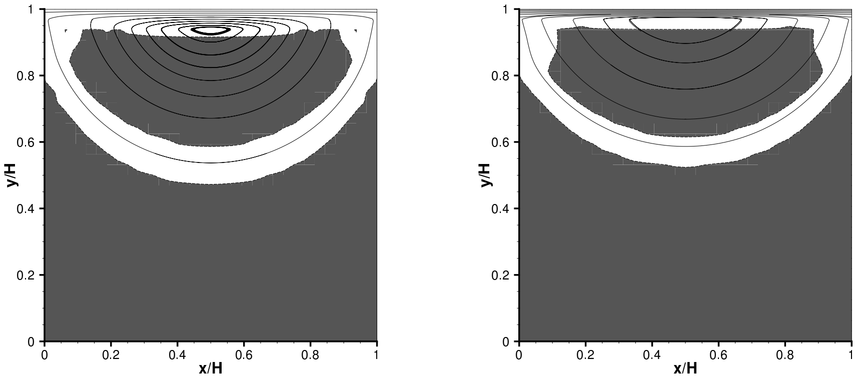

(e) $Bn = 200.0$ (f) $Bn = 500.0$

Figure 3.14: Growth of the unyielded zone

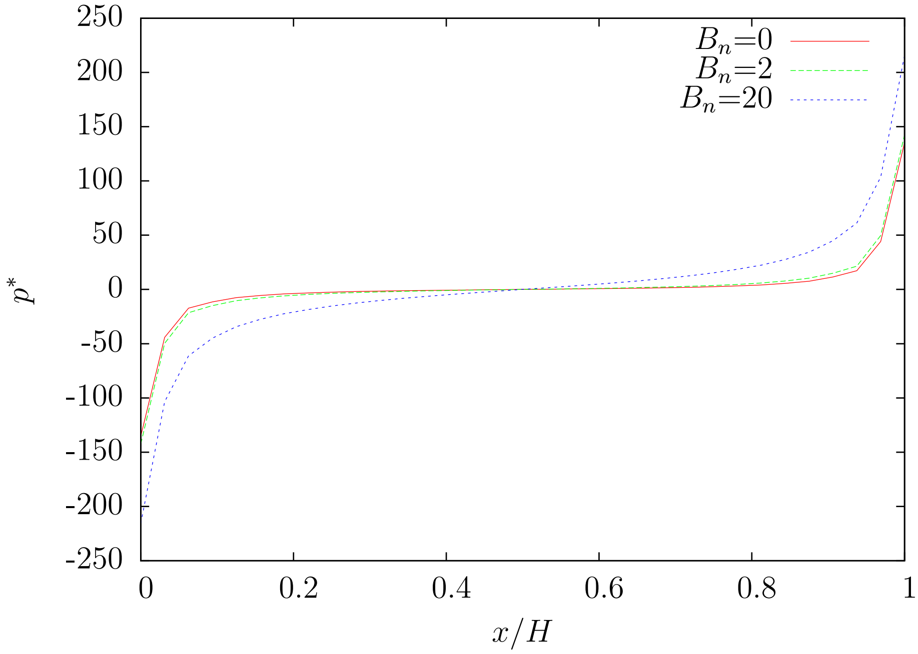

Figure 3.15: Pressure distribution along the lid

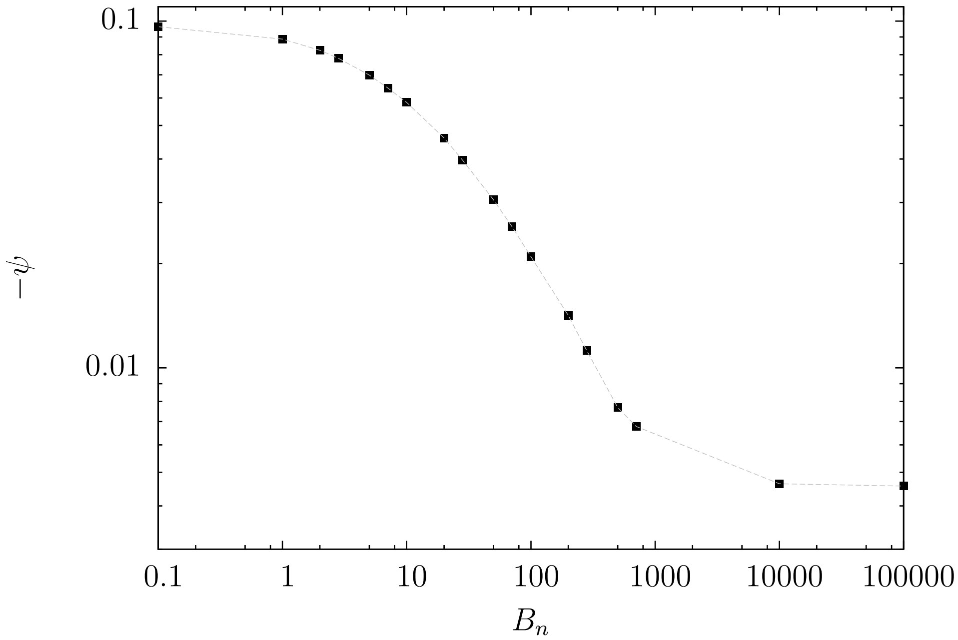

Figure 3.16: Vortex intensity

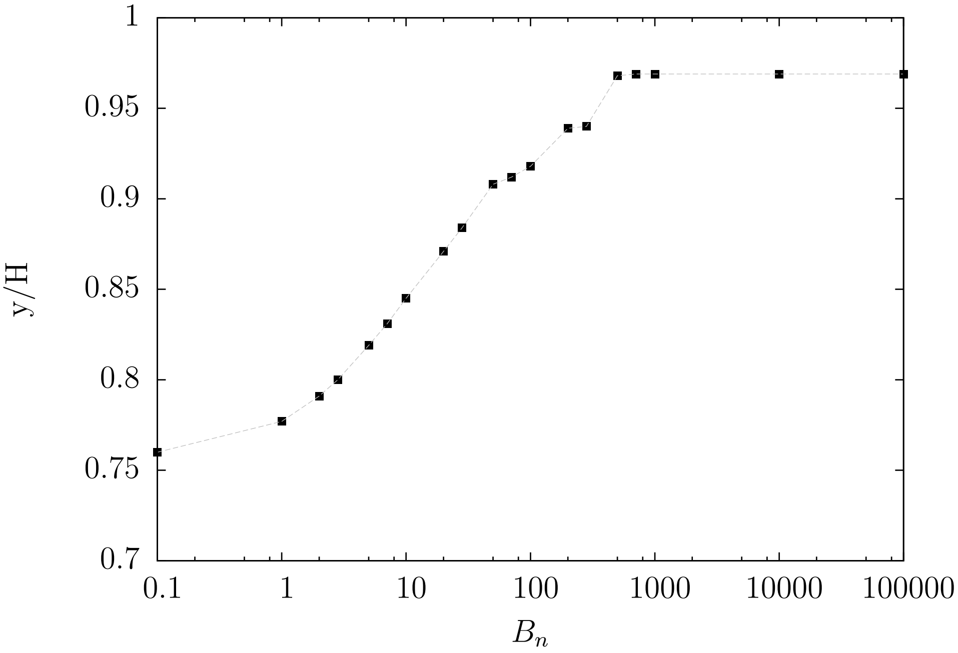

Figure 3.17: Vertical eye of the vortex position

3.6 Flow around cylinder

A flow around cylinder between two parallel plates is another example of common benchmark. Regarding the viscoplastic fluids, at least two variations of a problem were previously published in [47] and [29]. The first one assumes a Poiseuille flow velocity profile to appear in a large distance from the cylinder, while the flow is a pressure-driven and no-slip boundary conditions are prescribed on the plates. We've preformed similar simulations, but due to the rather vaguely defined dimensionless quantities, the results cannot be compared to our full satisfaction. Fortunately the second article describing flow of cylinder through viscoplastic fluid is clear in terms of used quantities and we present the results for the same problem as in [29].

The governing equations take the usual form of (3.30)–(3.34). We introduce dimensionless Bingham number Bn, dimensionless velocity $\boldsymbol{u}^*$ and dimensionless drag coefficient F_B^*.

$$Bn = \frac{\sqrt{2}g(2R)}{\eta U} \ , \quad \boldsymbol{u}^* = \frac{\boldsymbol{u}}{U} \ , \quad F_B^* = \frac{F_D}{\eta U L_C} \ , \tag{3.50}$$

where R is the cylinder radius, U is the x-component of the velocity far from the cylinder, F_D is the drag force acting on the cylinder (the x-component of the force acting on the cylinder) and L_C is the length of the cylinder in the cross-section.

Boundary conditions can be seen in Fig. 3.18, all around the channel there is a unit velocity in the direction of the channel and on the cylinder there is a no-slip condition.

$$u^* = 1 \ , \ v^* = 0 \qquad \text{on } \Gamma_1 \ , \tag{3.51}$$

$$\boldsymbol{u}^* = 0 \qquad \text{on } \Gamma_2 \ . \tag{3.52}$$

Velocity and viscosity were set as unity, the channel width ratio is $H/R = 2:1$ and the channel length ratio is $L/R = 12:1$. All the results presented show only the middle area of the channel around cylinder, since the areas of the inlet and outlet

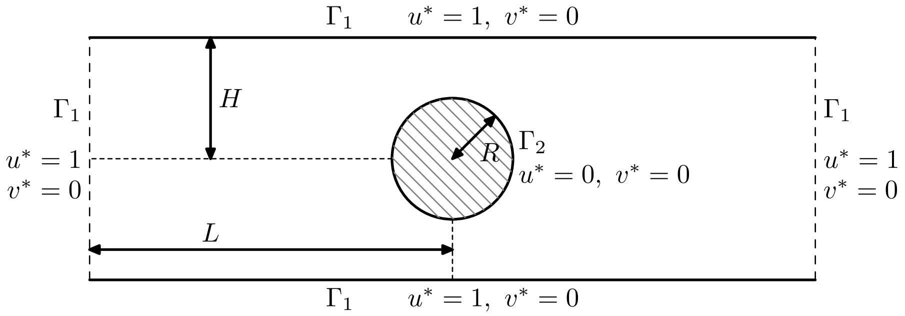

Figure 3.18: Boundary conditions

don't feature anything interesting. Used mesh is in Fig. 3.19. Bingham numbers range $0 \leq Bn \leq 1000$.

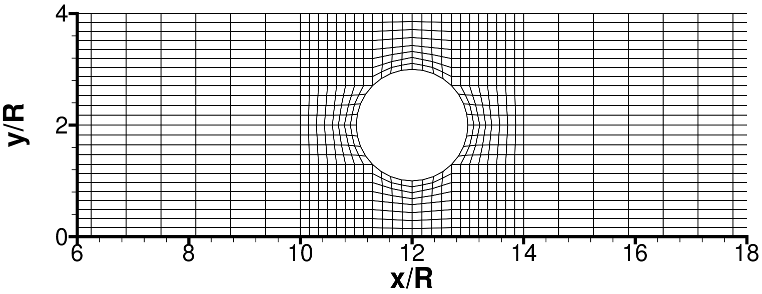

Figure 3.19: Used mesh

For the unyielded region visualisation the same procedure as for the lid-driven cavity is used. We start with Von Mises criterion and then proceed with $|\boldsymbol{D}|$ low that matches the results of Von Mises criterion. The limiting value was determined as 0.007, i.e dark areas in the following figures represents $|\boldsymbol{D}| < 0.007$. Our results in Fig. 3.20 match those in [29] quite well. Especially in the size of the larger unyielded area, the smaller ones by the cylinder seem to be bit larger in x-direction and smaller in y-direction in our case.

Additionally streamlines and isobars of Newtonian fluid and Bingham fluids with $Bn = 10$ and $Bn = 1000$ are in Fig. 3.21. Streamlines show us, how the Bingham fluid is getting closer to the cylinder and hence increasing the acting force.

Last comparison for the flow around cylinder is the relation between drag coefficient and Bingham number. The computed data were fitted in `gnuplot` by the equation

$$F_B^* = F_N^*(1 + aBn)^b \qquad 0 \leq Bn \leq 1000. \tag{3.53}$$

Fitting results are displayed in the box below. The value of F_N^* differ from the reported by less than 0.2%, value b by 1.6%, however parameter a is about 25% lower. Such difference shows us that in our case the acting force doesn't grow enough with rising Bingham number. This difference goes hand in hand with the different shapes of unyielded regions by the cylinder. Drag coefficient progress and fitting function are in Fig. 3.22.

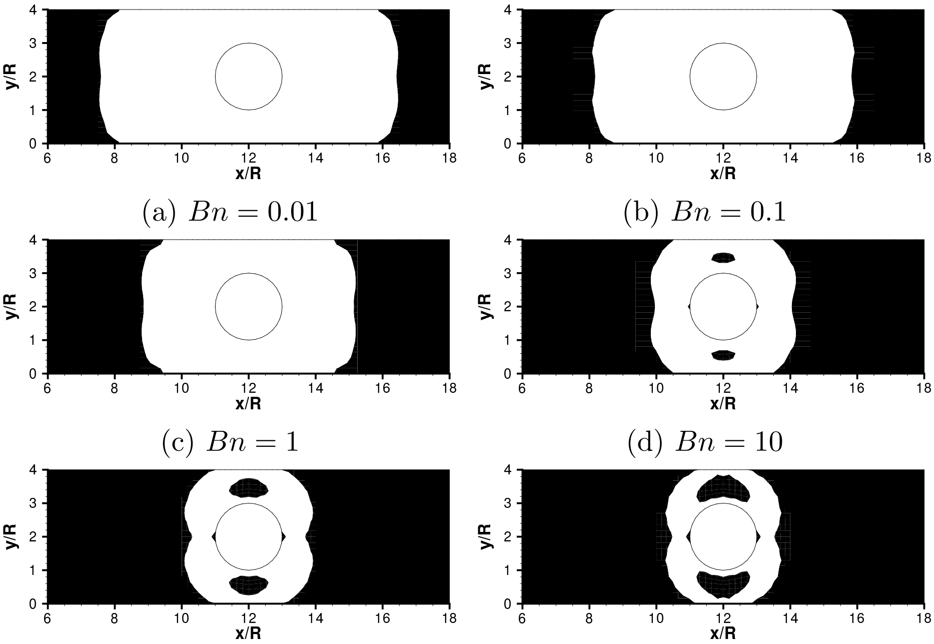

(a) $Bn = 0.01$ (b) $Bn = 0.1$

(c) $Bn = 1$ (d) $Bn = 10$

(e) $Bn = 100$ (f) $Bn = 1000$

Figure 3.20: Growth of unyielded region

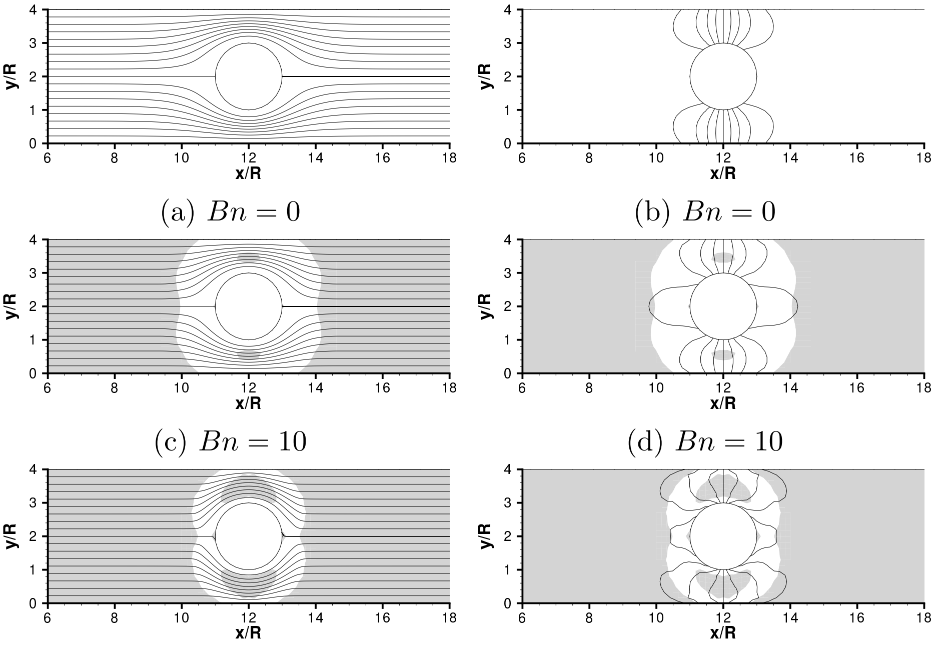

(a) $Bn = 0$ (b) $Bn = 0$

(c) $Bn = 10$ (d) $Bn = 10$

(e) $Bn = 1000$ (f) $Bn = 1000$

Figure 3.21: Streamlines on the left, isobars on the right

```
Final set of parameters            Asymptotic Standard Error
=======================            ==========================


F*_N            = 99.1766          +/- 0.8149         (0.8217%)
a               = 0.116953         +/- 0.001461       (1.249%)
b               = 0.955355         +/- 0.00129        (0.135%)
```

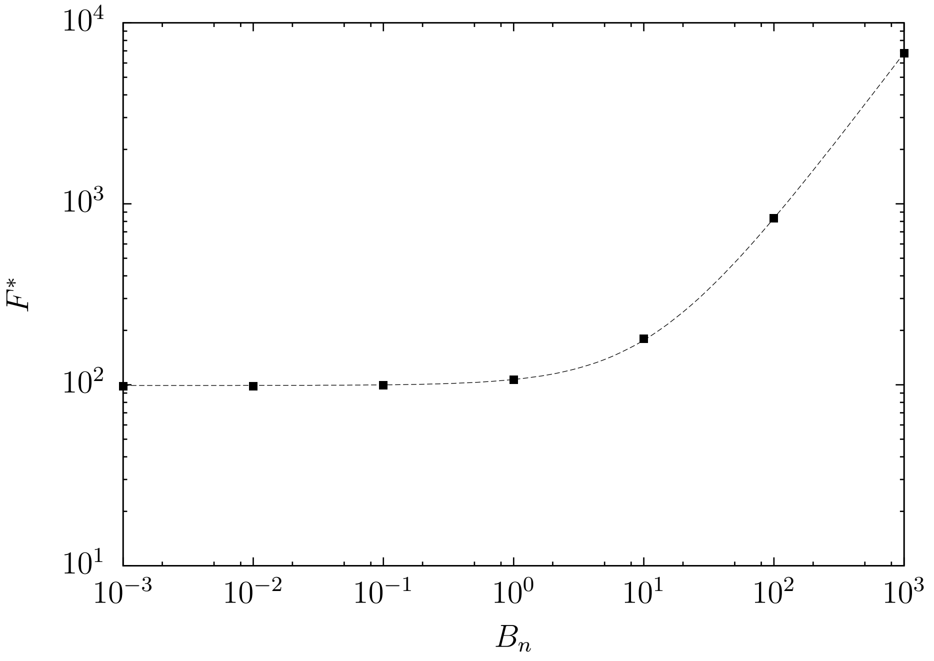

Figure 3.22: Drag coefficient

3.7 Wire-drawing problem

A similar problem was published in [25], however their domain $\Omega \in \mathbb{R}^3$ was reduced to (z, r) plane in cylindrical coordinates. Our simulation is as before in x, y plane. Governing equations are (3.30)–(3.34). In this case, we use the symmetry of the problem and compute only on the top half of the domain. Boundary conditions are shown in Fig. 3.23.

$$u \approx 14.3\,\mathrm{mm\,s^{-1}}\,,\ \mathrm{v} = 0 \qquad \text{on } \Gamma_1^{\mathrm{i}}\ , \tag{3.54}$$

$$u = 18.0\,\mathrm{mm\,s^{-1}}\,,\ \mathrm{v} = 0 \qquad \text{on } \Gamma_1^{\mathrm{o}}\ , \tag{3.55}$$

$$\frac{\partial u}{\partial y} = 0\,,\ v = 0 \qquad \text{on } \Gamma_2\ , \tag{3.56}$$

$$\boldsymbol{t}_\tau = 0\,,\ v = 0 \qquad \text{on } \Gamma_3\ , \tag{3.57}$$

$$\left.\begin{array}{l} \qquad\qquad \boldsymbol{u}\cdot\boldsymbol{\nu} = 0 \\ |\boldsymbol{t}_\tau| \le \mu S \left\{ \begin{array}{l} \text{if } |\boldsymbol{t}_\tau| < \mu S \text{ then } \boldsymbol{u}_\tau = 0 \\ \text{if } |\boldsymbol{t}_\tau| = \mu S \text{ then there exists } \lambda \ge 0 \\ \text{such that } \boldsymbol{u}_\tau = -\lambda \boldsymbol{t}_\tau \end{array}\right. \end{array}\right\} \text{on } \Gamma_4^l \cup \Gamma_4^d\ , \tag{3.58}$$

where $S = |\boldsymbol{T}'| = g + 2\eta|\boldsymbol{D}(\boldsymbol{u})|$. Boundaries Γ_4^l and Γ_4^d differ in μ.

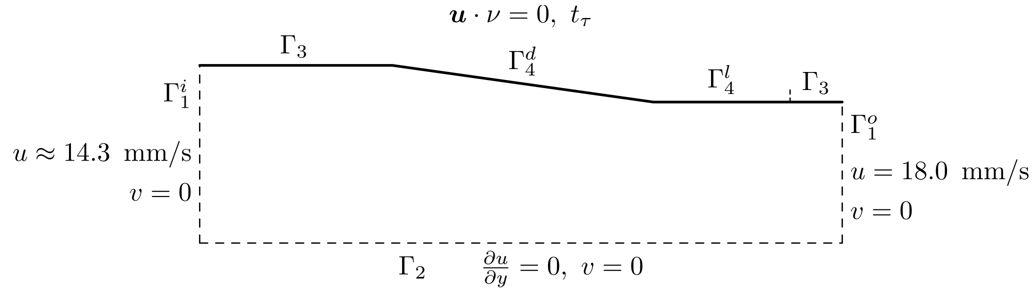

Figure 3.23: Boundary conditions

Actual data for the problem are $r_i = 0.47$ mm, $r_o = 0.373$ mm, which are the radii of the inlet and outlet. $\theta = 8°$ and the legth of the land is 0.362 mm. Velocity in inlet is chosen to satisfy an incompressibility condition. $\eta = 2.94\,\mathrm{N\,s\,mm^{-2}}$, $g = 289\,\mathrm{N\,mm^{-2}}$, $\mu^d = 0.09$ and $\mu^l = 0.08$. Used mesh is in Fig. 3.24.

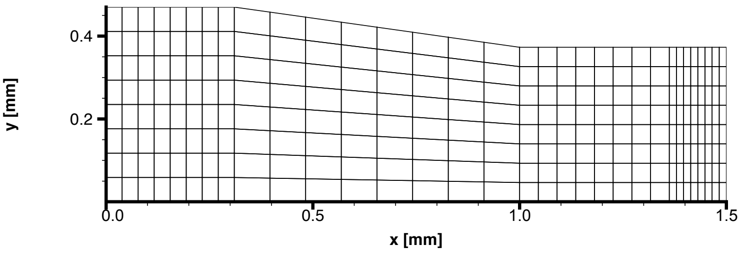

Figure 3.24: Used mesh

Computed streamlines are in Fig. 3.25a. Fig. 3.25b shows us how the velocity increases as the cone gets tighter, moreover the acceleration is delayed near the die surface because of the friction. Notice in Fig. 3.25c that the velocity component v is positive by the exit of the die, the wire is undergoing die swelling phenomenon. Fig. 3.25d shows what one would expect, wire enters and leaves the die as a rigid body, highest strain rates appears at the enter and the exit of the die.

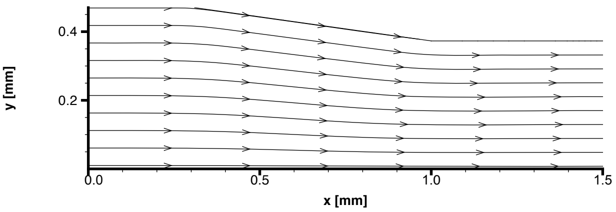

(a) Streamlines

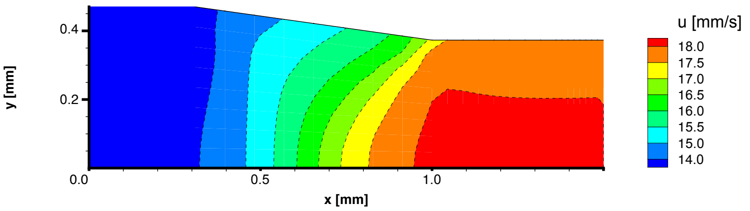

(b) Velocity component u

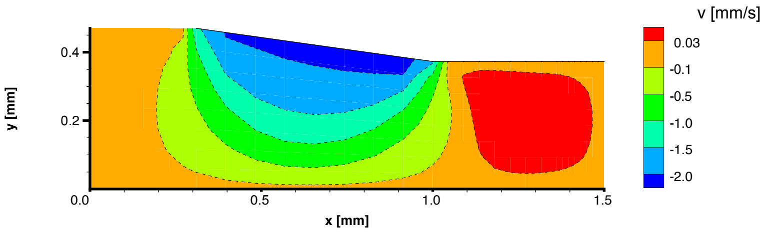

(c) Velocity component v

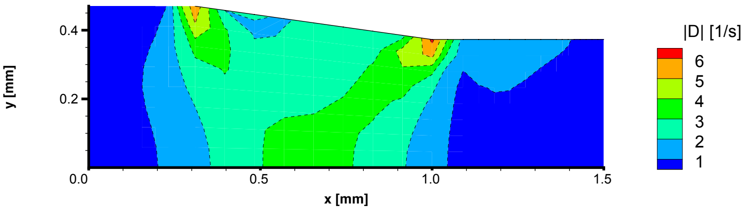

(d) Strain rate $|D|$

Figure 3.25: Wire-drawing problem results

Our simulations features the same phenomena as the results in [25], exact numbers cannot be compared due to the different coordinates, but even though we find the results satisfying.

3.8 Tape-casting unit

3.8.1 ALE finite element method

We shall derive governing equations in Arbitrary Lagrangian-Eulerian (ALE) formalism to allow us to solve free boundary problem. Nice introduction to ALE is in [41] and we follow first few pages to derive necessary transformations.

Free boundary problems can be solved using three types of numerical methods, Lagrangian, Eulerian and Arbitrary Lagrangian-Eulerian. In Lagrangian methods each point of free boundary moves with fluids. These methods are very accurate, but require often remeshing. Group of Eulerian methods places free boundary points into a fixed mesh. Such mesh must be refined enough to obtain sufficient accuracy. Also the equations are solved on the larger domain and the occupied one with the fluid may be distinguished by means of the characteristic function. ALE methods combine advantages of both approaches mentioned. Mesh nodes are related to the fluid velocity on the free boundary and inside the domain one an independent motion can be prescribed and frequent remeshing can be avoided.

The material body $\mathcal{B}$ occupies open region in $\mathbb{R}^n$. Let us denote Ω another open region in $\mathbb{R}^n$ as well and ϕ a motion of $\mathcal{B}$. $\boldsymbol{x} = \phi(\boldsymbol{X}, t)$ is the position of material point $\boldsymbol{X}$ at time t. The velocity and acceleration can be defined in a standard way

$$\boldsymbol{u}(\boldsymbol{x}, t) = \frac{\partial \phi}{\partial t}(\boldsymbol{X}, t) \ , \tag{3.59}$$

$$\boldsymbol{a}(\boldsymbol{x}, t) = \frac{\mathrm{d}\boldsymbol{u}}{\mathrm{d}t} \ . \tag{3.60}$$

$\hat{\boldsymbol{x}} \in \Omega$ follows referential motion λ to take a position $\boldsymbol{x} = \lambda(\hat{\boldsymbol{x}}, t)$. Its velocity is

$$\boldsymbol{w}(\boldsymbol{x}, t) = \frac{\partial \lambda}{\partial t}(\hat{\boldsymbol{x}}, t) \ . \tag{3.61}$$

Functions defined on Ω will be denoted with hat, i.e. $\boldsymbol{w}(\boldsymbol{x}, t) = \boldsymbol{w}(\lambda(\hat{\boldsymbol{x}}, t), t) = \hat{\boldsymbol{w}}(\hat{\boldsymbol{x}}, t)$. Then the updated referential configuration $\lambda_t(\Omega)$ is determined by the velocity field $\hat{\boldsymbol{w}}(\hat{\boldsymbol{x}}, t)$ or by the gradient deformation tensor

$$\hat{\boldsymbol{F}}_{ij} = \frac{\partial \boldsymbol{x}_i}{\partial \hat{\boldsymbol{x}}_j} \ . \tag{3.62}$$

A point occupying $\lambda_t(\Omega) \cap \phi_t(\mathcal{B})$ relates original points X and $\hat{\boldsymbol{x}}$ with the equation

$$\hat{\boldsymbol{x}} = \lambda^{-1}(\phi(\boldsymbol{X}, t), t) = \Psi(\boldsymbol{X}, t) \ . \tag{3.63}$$

The mapping Ψ is a motion of $\mathcal{B}$ over Ω. And it also holds

$$\boldsymbol{x} = \lambda(\Psi(\boldsymbol{X}, t), t) \ , \tag{3.64}$$

which after time differentiating results in

$$\boldsymbol{u}(\boldsymbol{x}, t) = \boldsymbol{w}(\boldsymbol{x}, t) + \hat{\boldsymbol{F}}(\hat{\boldsymbol{x}}, t) \cdot \bar{c}(\hat{x}, t) \ . \tag{3.65}$$

$\bar{c}$ is the relative velocity

$$\bar{c}(\hat{\boldsymbol{x}}, t) = \frac{\partial \Psi}{\partial t}(\boldsymbol{X}, t) \ . \tag{3.66}$$

The acceleration of point $\boldsymbol{X}$ as a function of $\hat{\boldsymbol{x}}$ is

$$\boldsymbol{a}(\boldsymbol{x}, t) = \hat{\boldsymbol{a}}(\hat{\boldsymbol{x}}, t) = \frac{\mathrm{d}\hat{\boldsymbol{u}}}{\mathrm{d}t} \ , \tag{3.67}$$

which can be expanded into

$$\hat{\boldsymbol{a}}(\hat{\boldsymbol{x}}, t) = \frac{\partial \hat{\boldsymbol{u}}}{\partial t}(\hat{\boldsymbol{x}}, t) + (\bar{c}(\hat{\boldsymbol{x}}, t) \cdot \hat{\nabla})\hat{\boldsymbol{u}}(\hat{\boldsymbol{x}}, t) \ , \tag{3.68}$$

where $\hat{\nabla}$ denoted gradient operator in the $\hat{\boldsymbol{x}}$ coordinates. With (3.65) we can rewrite last equation as

$$\hat{\boldsymbol{a}}(\hat{\boldsymbol{x}}, t) = \frac{\partial \hat{\boldsymbol{u}}}{\partial t}(\hat{\boldsymbol{x}}, t) + [(\hat{\boldsymbol{F}}^{-1} \cdot (\hat{\boldsymbol{u}} - \hat{\boldsymbol{w}})) \cdot \hat{\nabla}]\hat{\boldsymbol{u}}(\hat{\boldsymbol{x}}, t) \ . \tag{3.69}$$

We can now reformulate basic conservation equations. Let us start with the momentum equation in form

$$\rho(\boldsymbol{x}, t)\boldsymbol{a}(\boldsymbol{x}, t) = \boldsymbol{b}(\boldsymbol{x}, t) + \operatorname{div} \boldsymbol{T}(\boldsymbol{x}, t) \ , \tag{3.70}$$

ρ denotes the density, $\boldsymbol{b}$ the body forces and $\boldsymbol{T}$ is the Cauchy stress tensor. Changing the coordinates into $\hat{\boldsymbol{x}}$ transforms the last equation in

$$\hat{\rho}(\hat{\boldsymbol{x}}, t)\hat{J}\hat{\boldsymbol{a}}(\hat{\boldsymbol{x}}, t) = \hat{J}\hat{\boldsymbol{b}}(\hat{\boldsymbol{x}}, t) + \hat{\operatorname{div}}(\hat{J}\boldsymbol{T}(\hat{\boldsymbol{F}}^{-T})) \ , \tag{3.71}$$

$\hat{J} = \det \boldsymbol{F}$. $\hat{\boldsymbol{a}}(\hat{\boldsymbol{x}}, t)$ can be substituted from (3.69),

$$\hat{\rho}(\hat{\boldsymbol{x}}, t)\hat{J}\left(\frac{\partial \hat{\boldsymbol{u}}}{\partial t}(\hat{\boldsymbol{x}}, t) + [(\hat{\boldsymbol{F}}^{-1} \cdot (\hat{\boldsymbol{u}} - \hat{\boldsymbol{w}})) \cdot \hat{\nabla}]\hat{\boldsymbol{u}}(\hat{\boldsymbol{x}}, t)\right) = \hat{J}\hat{\boldsymbol{b}}(\hat{\boldsymbol{x}}, t) + \hat{\operatorname{div}}(\hat{J}\boldsymbol{T}(\hat{\boldsymbol{F}}^{-T})) \ . \tag{3.72}$$

Conservation of mass takes after transformation following form

$$\hat{J}\frac{\partial \hat{\rho}}{\partial t} + \hat{\operatorname{div}}(\hat{\rho}\hat{J}\hat{\boldsymbol{F}}^{-1}\hat{\boldsymbol{u}}) = 0. \tag{3.73}$$

3.8.2 Simulation results

Following numerical simulation based on the experimental data as in [28] aims to determine the shape of free surface at the exit of tape-casting machine and also describe the flow behaviour in the reservoir. Unlike the other simulations, governing equations had to be modified for use of ALE method. As the Reynolds number (3.78) is in all three cases of the order 10^{-3} we will omit the inertia. Apart from the other unknowns in $\boldsymbol{u}$-p-$\boldsymbol{S}$-$\boldsymbol{D}$ formulation, we introduce the mesh velocity $\boldsymbol{w}$, the governing equations are

$$\hat{\operatorname{div}}(\hat{J}\boldsymbol{T}'(\hat{\boldsymbol{F}}^{-T})) + \hat{J}\hat{\boldsymbol{g}}(\hat{\boldsymbol{x}}) = 0 \ , \tag{3.74}$$

$$\hat{\operatorname{div}}(\hat{\rho}\hat{J}\hat{\boldsymbol{F}}^{-1}\hat{\boldsymbol{u}}) = 0 \ , \tag{3.75}$$

$$\Delta \boldsymbol{w} = 0 \ , \tag{3.76}$$

$$\boldsymbol{T}'|\boldsymbol{D}_\varepsilon| - 2\eta \boldsymbol{D}|\boldsymbol{D}_\varepsilon| + g\boldsymbol{D} = 0 \ , \tag{3.77}$$

with Frobenius norm (3.34).

Boundary conditions are on Fig. 3.26. Along the border AB the tangential velocity is prescribed, along the exit BC no surface tractions are imposed and $v = 0$. Along the free surface CD a no-cross boundary condition is imposed and also surface tension effect are omitted. On both boundaries DE and EF a no-slip boundary condition is present. Along the reservoir inlet FG no surface traction a $u = 0$ are imposed. The reservoir wall GA has again no-slip velocity condition. The discontinuity of velocity in point A is again solved by the interpolation on the bottom element of GA boundary.

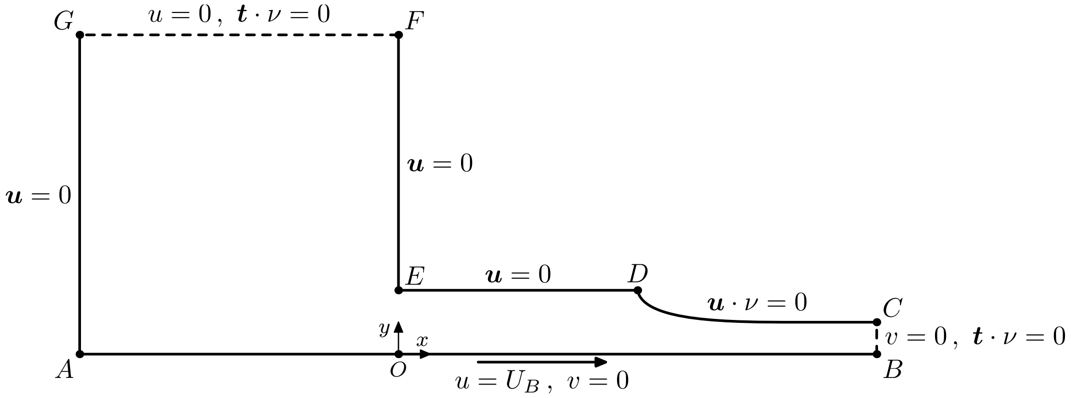

Figure 3.26: Tape-casting machine boundary conditions

The geometrical dimensions of the experiment are in Fig. 1.11. The speed of belt is kept at constant value $U_B = 7.58\,\mathrm{mm\,s^{-1}}$. The slurry density was measured at $\rho = 1825.5 \pm 0.7\,\mathrm{kg\,m^{-3}}$. Yield stress found by extrapolation is $g = 12.1\,\mathrm{Pa}$ and the material viscosity $\eta = 4.46\,\mathrm{Pa\,s}$. All measurements were carried at 20℃. Apart from this setting (Case II), also belt speeds $3.79\,\mathrm{mm\,s^{-1}}$ (Case I) and $15,18\,\mathrm{mm\,s^{-1}}$ (Case III) were considered.

The dimensionless Reynolds number is defined as

$$Re = \frac{\rho U_B h}{\mu}\ . \tag{3.78}$$

All numerical simulations were carried on mesh shown in Fig. 3.27, the mesh in the channel is uniform and exactly same as its shown part in the figure. Simulations started on the fixed mesh with Newtonian fluid, then continued on fixed mesh until numerical solution for Bingham fluid was found and only after that the ALE method with moving nodes took part. Such procedure led to a fast convergence without any problems. The results are presented in figures 3.28. As a condition for unyielded region combination of Von Mises criterion and $|\boldsymbol{D}| < \epsilon$ were used, see section 3.5 for more details. In this case $|\boldsymbol{D}| < 0.01$ are used, such high value is a result of coarse mesh grid. Due to the coarse mesh in the reservoir only main characteristics in unyielded regions were rendered, the exact position shown isn't absolutely reliable. Our main focus was aimed at the area of exit, where there are experimental data available. In comparison with results published in [28], our seem to capture the shape of free boundary better, used meshes were approximately same.

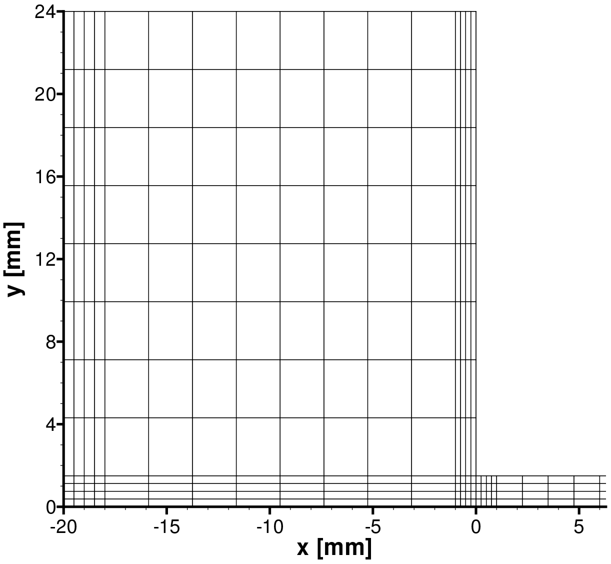

Figure 3.27: Used mesh, reservoir

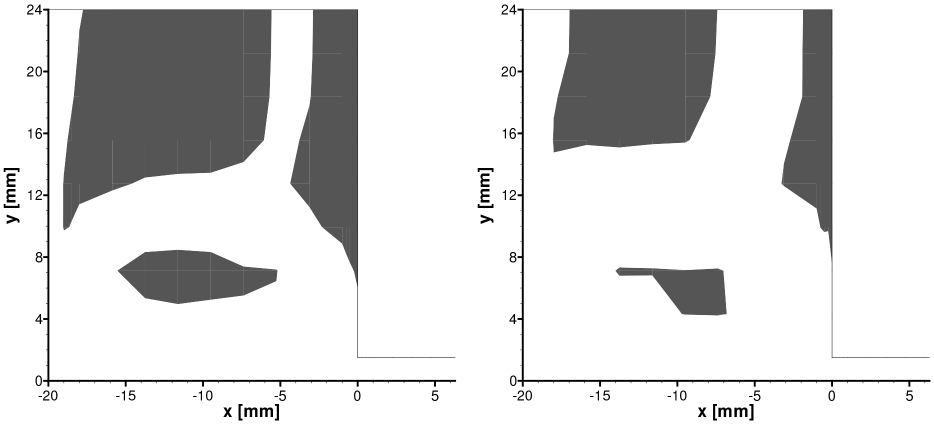

(a) Case I reservoir

(b) Case II reservoir

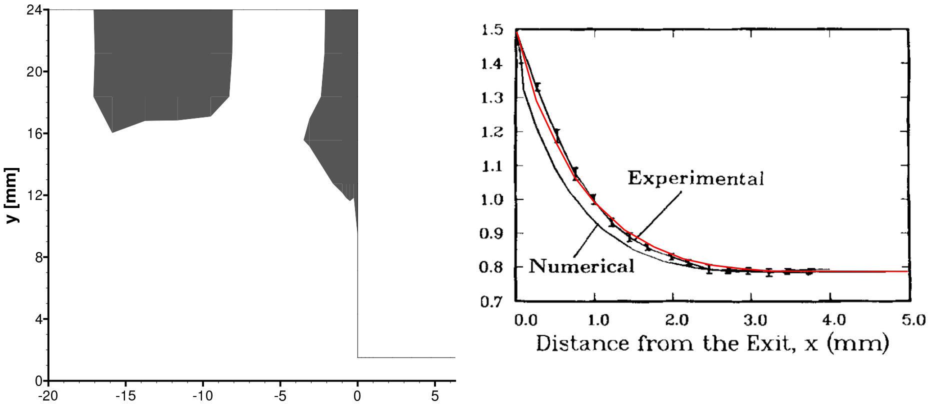

(c) Case III reservoir

(d) Case II exit, our results are displayed with the red line (original figure from [28])

Figure 3.28: Tape-casting, results

3.9 Herschel-Bulkley fluid

Apart from Bingham fluid previously mentioned process is also applicable to other fluid models. One of the models most resembling Bingham fluid is Herschel-Bulkley fluid. It extends Bingham fluid with shear-thinning / shear-thickening property. The constitutive equation is

$$\left.\begin{array}{lr} \boldsymbol{T}' = 2\eta|\boldsymbol{D}|^{r-2}\boldsymbol{D} + g\frac{\boldsymbol{D}}{|\boldsymbol{D}|} & \text{if } |\boldsymbol{D}| \neq 0 \\ |\boldsymbol{T}'| \leq g & \text{if } |\boldsymbol{D}| = 0\ . \end{array}\right\} \tag{3.79}$$

Herschel-Bulkley fluid reduces to a Bingham fluid for $r = 2$.

The only difference in modelling flows of Herschel-Bulkley fluid is that for r distant from 2 more iterations in r are needed, however convergence and precision properties remains similar to those presented in section 3.4.

The main drawback considering our aims is less available results for comparing both benchmark problems and more perceptibly problems from common industry. Let us just present short illustration of shear-thinning and shear-thickening effect on Bingham fluid in Poiseuille flow. Governing equations alter only in constitutive equations, i.e. the system is described with (3.30), (3.31), (3.34) and

$$\boldsymbol{T}'|\boldsymbol{D}_\varepsilon| - 2\eta|\boldsymbol{D}|^{r-2}\boldsymbol{D}|\boldsymbol{D}_\varepsilon| + g\boldsymbol{D} = 0\ , \tag{3.80}$$

where $|\boldsymbol{D}_\varepsilon| = \sqrt{|\boldsymbol{D}|^2 + \varepsilon^2}$.

Boundary conditions are same as in section 3.4, i.e. (3.36)–(3.38) and Fig. 3.2. Also the used mesh is same with 2048 elements.

For the proper description it remains to introduce dimensionless velocity $\boldsymbol{u}^*$ and dimensionless yield stress g^*,

$$u^* = \frac{\boldsymbol{u}}{U_N}\ , \qquad g^* = \frac{\sqrt{2}gH}{\eta U_N}\ , \tag{3.81}$$

U_N is maximal velocity of Newtonian fluid in the considered problem, channel width and viscosity are unit. Fig. 3.29 presents velocity profiles for Newtonian fluid, Bingham fluid ($g^* = 2.3$) and Herschel-Bulkley fluid ($g^* = 2.3$, $r = 1.8$ and 2.2).

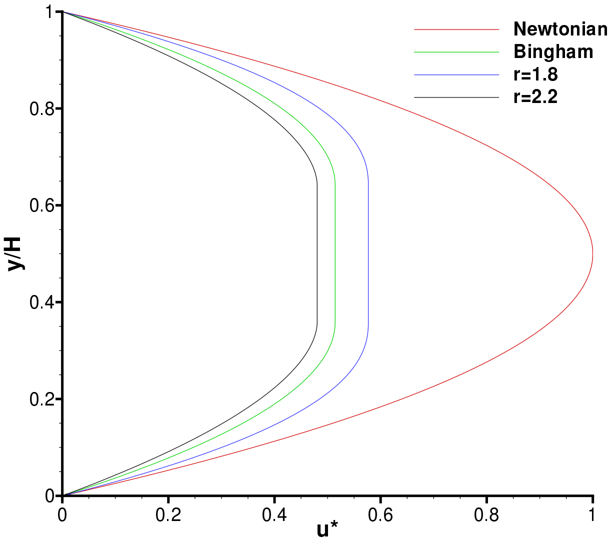

Figure 3.29: Velocity profiles, except Newtonian fluid ($g^* = 0$), $g^* = 2.3$

Conclusion

Finite element simulations have been undertaken for several different problems. We managed to improve our previous, mostly unsuccessful, results we were able to achieve. At the end we have a quite simple method, how to enrich a common primal mixed formulation in a standard finite element implementation and obtain a robust system for solving problems of visco-plastic flows. The results are comparable with those presented in many articles.

We see the main disadvantage in higher computational requirements as in terms of CPU time and memory usage. However we believe that given the current state of computer technology, this shouldn't be much of an issue. On the other hand results acquired by Mitsoulis and Zisis [29], [30] and [47] covered the same range of Bingham numbers and should be much less hardware demanding. Unfortunately we weren't able to reproduce their approach.

Concerning the visco-plastic materials, possible future efforts might try to reduce zig-zag phenomenon. Doing so would primarily lead to more accurate yield surface detection. Another possible field of development is tailoring a special preconditioner and reducing the required number of iterations and more importantly the regularization parameter stepping.

Moreover we hope that presented results could be a valuable source of data for modelling materials described by implicit constitutive relations. We hope that used approaches could be potentially modified to better fit new material models and that the established framework could join the results achieved in the field of analysis.

Bibliography

[1] 1911 Encyclopædia Britannica — Wikisource, The Free Library. Wire, 2011. [Online; accessed 1-August-2012].

[2] S.S. Abdali, E. Mitsoulis, and N.C. Markatos. Entry and exit flows of bingham fluids. *Journal of Rheology*, 36:389, 1992.

[3] A. Aposporidis, E. Haber, M.A. Olshanskii, and A. Veneziani. A mixed formulation of the bingham fluid flow problem: Analysis and numerical solution. *Computer Methods in Applied Mechanics and Engineering*, 2011.

[4] F. P. T. Baaijens. Mixed finite element methods for viscoelastic flow analysis: a review1. *Journal of Non-Newtonian Fluid Mechanics*, 79(2-3):361–385, 1998.

[5] J. Baranger and D. Sandri. Finite element method for the approximation of viscoelastic fluid flow with a differential constitutive law. In *Computational Fluid Dynamics' 92*, volume 1, pages 1021–1025, 1992.

[6] J. Baranger and D. Sandri. A formulation of stokes's problem and the linear elasticity equations suggested by the oldroyd model for viscoelastic flow. *Modélisation mathématique et analyse numérique*, 26(2):331–345, 1992.

[7] M.A. Behr, L.P. Franca, and T.E. Tezduyar. Stabilized finite element methods for the velocity-pressure-stress formulation of incompressible flows. *Computer Methods in Applied Mechanics and Engineering*, 104(1):31–48, 1993.

[8] M. Bercovier and M. Engelman. A finite-element method for incompressible non-newtonian flows. *Journal of Computational Physics*, 36(3):313–326, 1980.

[9] E.C. Bingham. *Fluidity and plasticity.* McGraw-Hill New York, 1922.

[10] M. Bulíček. Implicit constitutive theory: from analysis through model reduction towards efficient numerical methods, Part IV: Mathematical analysis. SNA '12.

[11] M. Bulíček, P. Gwiazda, J. Málek, K.R. Rajagopal, and A. Swierczewska-Gwiazda. On flows of fluids described by an implicit constitutive equation characterized by a maximal monotone graph, in "mathematical aspects of fluid mechanics". *London Mathematical Society Lecture Note Series, Cambridge University Press, to appear*, 2012.

[12] M. Bulíček, P. Gwiazda, J. Málek, and A. Swierczewska-Gwiazda. On unsteady flows of implicitly constituted incompressible fluids. *Nečas Center for Mathematical Modeling, Preprint no. 2011-008*, 2011.

[13] CFD Online. Lid-driven cavity problem, 2008. [Online; accessed 1-August-2012].

[14] M. Chatzimina, C. Xenophontos, G.C. Georgiou, I. Argyropaidas, and E. Mitsoulis. Cessation of annular poiseuille flows of bingham plastics. *Journal of non-newtonian fluid mechanics*, 142(1):135–142, 2007.

[15] P. Coussot. *Rheometry of pastes, suspensions, and granular materials.* Wiley Online Library, 2005.

[16] N. Cristescu. *Dynamic plasticity*, volume 10. World Scientific Pub Co Inc, 2007.

[17] H. Damanik, J. Hron, A. Ouazzi, and S. Turek. A monolithic fem-multigrid solver for non-isothermal incompressible flow on general meshes. *Journal of Computational Physics*, 228(10):3869–3881, 2009.

[18] E.J. Dean, R. Glowinski, and G. Guidoboni. On the numerical simulation of bingham visco-plastic flow: Old and new results. *Journal of non-newtonian fluid mechanics*, 142(1):36–62, 2007.

[19] P.W. Egolf and M. Kauffeld. From physical properties of ice slurries to industrial ice slurry applications. *International Journal of Refrigeration*, 28(1):4–12, 2005.

[20] Featflow. Dfg flow around cylinder, laminar case (re=20). [Online; accessed 1-August-2012].

[21] M. Fortin and R. Pierre. On the convergence of the mixed method of crochet and marchal for viscoelastic flows. *COMP. METHODS APPL. MECH. ENG.*, 73(3):341–350, 1989.

[22] R.J. Goldstein. *Fluid mechanics measurements.* Hemisphere Publishing Corporation, New York, 1983.

[23] J.S. Howell and N.J. Walkington. Inf–sup conditions for twofold saddle point problems. *Numerische Mathematik*, pages 1–31, 2009.

[24] J. Hron and S. Turek. A monolithic fem/multigrid solver for an ale formulation of fluid-structure interaction with applications in biomechanics. *Fluid-Structure Interaction*, pages 146–170, 2006.

[25] I.R. Ionescu and M. Sofonea. *Functional and numerical methods in viscoplasticity.* Oxford University Press Oxford, 1993.

[26] V. John and G. Matthies. Higher-order finite element discretizations in a benchmark problem for incompressible flows. *International Journal for Numerical Methods in Fluids*, 37(8):885–903, 2001.

[27] A. Kitanovski, D. Vuarnoz, D. Ata-Caesar, P.W. Egolf, T.M. Hansen, and C. Doetsch. The fluid dynamics of ice slurry. *International journal of refrigeration*, 28(1):37–50, 2005.

[28] H. Loest, R. Lipp, and E. Mitsoulis. Numerical flow simulation of viscoplastic slurries and design criteria for a tape casting unit. *Journal of the American Ceramic Society*, 77(1):254–262, 1994.

[29] E. Mitsoulis. On creeping drag flow of a viscoplastic fluid past a circular cylinder: wall effects. *Chemical engineering science*, 59(4):789–800, 2004.

[30] E. Mitsoulis and T. Zisis. Short communication flow of bingham plastics in a lid-driven square cavity. *Journal of non-newtonian fluid mechanics*, 101(1):173–180, 2001.

[31] J. Málek. Mathematical properties of flows of incompressible power-law-like fluids that are described by implicit constitutive relations. *Electronic Transactions on Numerical Analysis*, 31:110–125, 2008.

[32] J.G. Oldroyd. A rational formulation of the equations of plastic flow for a bingham solid. In *Mathematical Proceedings of the Cambridge Philosophical Society*, volume 43, pages 100–105. Cambridge Univ Press, 1947.

[33] J.G. Oldroyd. Two-dimensional plastic flow of a bingham solid. In *Mathematical Proceedings of the Cambridge Philosophical Society*, volume 43, pages 383–395. Cambridge Univ Press, 1947.

[34] M.A. Olshanskii. Analysis of semi-staggered finite-difference method with application to bingham flows. *Computer Methods in Applied Mechanics and Engineering*, 198(9-12):975–985, 2009.

[35] T.C. Papanastasiou. Flows of materials with yield. *Journal of Rheology*, 31:385, 1987.

[36] W. Prager. *Introduction to mechanics of continua.* Ginn, Boston, 1961.

[37] K.R. Rajagopal. On implicit constitutive theories. *Applications of Mathematics*, 48(4):279–319, 2003.

[38] K.R. Rajagopal. On implicit constitutive theories for fluids. *Journal of Fluid Mechanics*, 550:243–250, 2006.

[39] M. Reiner and S.F. Rheology. Handbuch der physik. *Springer, Berlin*, 6:457, 1958.

[40] R. Ridel and I-Wei Chen. *Ceramics Science and Technology: Vol. 3: Synthesis and Processing.* Wiley VCH, 2011.

[41] A. Soulaimani and Y. Saad. An arbitrary lagrangian-eulerian finite element method for solving three-dimensional free surface flows. *Computer methods in applied mechanics and engineering*, 162(1):79–106, 1998.

[42] G.G. Stokes. On the effect of the internal friction of fluids on the motion of pendulums. *Transactions of the Cambridge Philosophical Society*, IX., 1850.

[43] T. Udomphol. Mechanical metallurgy course, 2007. Suranaree University of Technology.

[44] M.B. Villas-Boas. Paradox de stokes: Uma nova abordagem. *8° Congreso Iberoamericano de Ingenieria Mecanica*, 2007.

[45] D. Vola, L. Boscardin, and JC Latché. Laminar unsteady flows of bingham fluids: a numerical strategy and some benchmark results. *Journal of Computational Physics*, 187(2):441–456, 2003.

[46] Wikipedia. File:Toothpaste.png — Wikipedia, The Free Encyclopedia, 2006. [Online; accessed 14-July-2012].

[47] T. Zisis and E. Mitsoulis. Viscoplastic flow around a cylinder kept between parallel plates. *Journal of non-newtonian fluid mechanics*, 105(1):1–20, 2002.

List of Tables

List of Figures

Attachments

1 Nonlinear iterations in convergence test

	H/h					
ε	16	32	64	128	256	512
1e-1	6	6	6	6	6	6
1e-2	8	25	9	8	8	8
1e-3	8	10	22	46		
1e-4	8	12	25			
1e-5	8	12	25			
1e-6	8	12	25			
1e-7	8	12	25			
1e-8	8	12	25			

	H/h					
ε	16	32	64	128	256	512
1e-1	2	2	2	2	3	3
1e-2	2	2	2	2	3	3
1e-3	2	2	2	2	4	5
1e-4	3	2	2	3	6	20
1e-5	3	3	3	4		
1e-6		3				
1e-7						
1e-8						

Table 3.5: Number of nonlinear iterations, $\boldsymbol{u}$-p-$\boldsymbol{S}$, Q_2, `T` (left), `D` (right)

	H/h					
ε	16	32	64	128	256	512
1e-1	6	6	6	6	6	6
1e-2	8	8	8	8	8	
1e-3	9	9	10	10		
1e-4	8	31				
1e-5	25					
1e-6						
1e-7						
1e-8						

	H/h					
ε	16	32	64	128	256	512
1e-1	5	2	2	2	3	5
1e-2	5	17	5	7	6	5
1e-3	5	14	7			
1e-4	5		6			
1e-5	5					
1e-6						
1e-7						
1e-8						

Table 3.6: Number of nonlinear iterations, $\boldsymbol{u}$-p-$\boldsymbol{S}$, Q_{2*}^{disc}, `T` (left), `D` (right)

	H/h					
ε	16	32	64	128	256	512
1e-1	6	6	6	6	6	6
1e-2	8	8	8	8	8	8
1e-3	9	10	9	9	10	10
1e-4	11	11	16	13	10	10
1e-5	20	9	25	28	19	21
1e-6	19	9	25	22	17	28
1e-7	20	9	25	23	16	23
1e-8	23	9	25			18

	H/h					
ε	16	32	64	128	256	512
1e-1	2	2	2	2		
1e-2	2	2	2	2		
1e-3	2	2	2	2		
1e-4	2	2	3	2		
1e-5		2	3			
1e-6		3				
1e-7		3				
1e-8						

Table 3.7: Number of nonlinear iterations, $\boldsymbol{u}$-p-$\boldsymbol{S}$-$\boldsymbol{D}$, Q_2, `T` (left), `D` (right)

	H/h					
ε	16	32	64	128	256	512
1e-1	6	6	6	6	6	6
1e-2	8	8	8	8	8	8
1e-3	9	9	10	9	10	10
1e-4	8	30	11	23	11	11
1e-5	9	12	16	43		
1e-6	9	13				
1e-7	8	12				
1e-8	8	10				

	H/h					
ε	16	32	64	128	256	512
1e-1	5	2	2	2	3	5
1e-2	5	17	5	6	5	3
1e-3	5	14	6		14	
1e-4	5	38	6			
1e-5	5		17			
1e-6	7					
1e-7						
1e-8						

Table 3.8: Number of nonlinear iterations, $\boldsymbol{u}$-p-$\boldsymbol{S}$-$\boldsymbol{D}$, Q_{2*}^{disc}, `T` (left), `D` (right)